Biogeosciences, 22, 6937–6962, 2025 https://doi.org/10.5194/bg-22-6937-2025 © Author(s) 2025. This work is distributed under the Creative Commons Attribution 4.0 License.





Evaluating the carbon and nitrogen cycles of the QUINCY terrestrial biosphere model using space-born optical remotely-sensed data

 $\label{eq:continuous} \textbf{Tuuli Miinalainen}^{1,2,3}, \textbf{Amanda Ojasalo}^{1,4}, \textbf{Holly Croft}^5, \textbf{Mika Aurela}^2, \textbf{Mikko Peltoniemi}^6, \textbf{Silvia Caldararu}^7, \textbf{S\"{o}nke Zaehle}^3, \textbf{and Tea Thum}^2$

Hans-Knöll-Straße 10, 07745 Jena, Germany

Correspondence: Tuuli Miinalainen (tuuli.miinalainen@fmi.fi)

Received: 23 June 2025 - Discussion started: 10 July 2025

Revised: 7 October 2025 - Accepted: 15 October 2025 - Published: 19 November 2025

Abstract. Accurate estimates of future land carbon sinks and thus the remaining carbon budget to achieve the Paris climate goals requires rigorous modelling of the carbon sequestration potential of the terrestrial biosphere. Estimating the terrestrial carbon budget requires an accurate understanding of the interlinkages between the land carbon and nitrogen cycles, yet coupled carbon-nitrogen cycle models exhibit large uncertainties. Leaf chlorophyll, chl_{leaf}, is an indicator of the leaf nitrogen content stored within photosynthetic nitrogen pools and is central to the exchange of carbon, water and energy between the biosphere and the atmosphere. In this work, we harness an advanced remote sensing (RS) chl_{leaf} product to evaluate a terrestrial biosphere model (TBM), QUantifying Interactions between terrestrial Nutrient CYcles and the climate system (QUINCY), which explicitly models chl_{leaf}. We focus on comparing the spatial and seasonal patterns of modelled and observed chlleaf, and then further assessing if modelled leaf area and productivity agree with a RS leaf area index product and in-situ eddy covariance-based gross primary production, respectively. In addition, we conduct additional simulations to test two alternative formulations of leaf-internal nitrogen allocation within QUINCY. Our analysis over a globally representative set of locations reveals that

QUINCY chl_{leaf} magnitudes are mostly in line with the RS chlleaf values. However, QUINCY chlleaf tends to show a narrower numerical range compared to RS for specific ecosystem types, such as grasslands. While the seasonal cycle of QUINCY chl_{leaf} mostly corresponds well to the observations, for many deciduous forests, the increase in QUINCY's chl_{leaf} predictions in spring and the decrease in autumn were delayed compared to observations. Our results also show that compared to the original leaf nitrogen allocation scheme of QUINCY, the revised scheme produced a more reasonable sensitivity of gross primary production to increases in chl_{leaf}. However, the revised scheme did not directly lead to improvement in simulating chlleaf and gross primary production. Our study shows the value of RS products linked to nitrogen cycle that will be useful in both carbon and nitrogen modelling, and paves way for closer linking of RS and TBMs.

1 Introduction

The terrestrial biosphere currently takes up approximately one-third of the anthropogenic fossil fuel carbon emissions

¹Earth Observation Research, Finnish Meteorological Institute, P.O. Box 503, 00101 Helsinki, Finland

²Climate System Research, Finnish Meteorological Institute, P.O. Box 503, 00101 Helsinki, Finland

³Department of Biogeochemical Signals, Max Planck Institute for Biogeochemistry,

⁴Department of Geosciences and Geography, University of Helsinki, Gustaf Hällströmin katu 2, 00560 Helsinki, Finland

⁵School of Biosciences, University of Sheffield, Western Bank, Sheffield, S10 2TN, UK

⁶Natural Resources Institute Finland (Luke), Latokartanonkaari 9, 00790 Helsinki, Finland

⁷Discipline of Botany, School of Natural Sciences, Trinity College Dublin, College Green, Dublin 2, Ireland

(Friedlingstein et al., 2023), and thereby playing pivotal role in slowing global climate warming (Nabuurs et al., 2022). The carbon (C) cycle is closely linked to the terrestrial nitrogen (N) cycle, as photosynthesis and plant growth require sufficient nutrient supply. Land carbon uptake is limited by nitrogen in many ecosystems (LeBauer and Treseder, 2008; Fisher et al., 2012; Tamm, 1991; Vitousek and Howarth, 1991; Ziehn et al., 2021), however, the magnitude of this limitation remains unclear. This highlights the need to better understand the coupled C and N cycles (Seiler et al., 2024), as future changes in climate will also affect these cycles (Arora et al., 2020).

Terrestrial biosphere models (TBMs) can be used to simulate coupled C and nutrient cycles and land-atmosphere interactions under a changing climate. In recent decades, TBMs have taken in an increasing number of factors affecting plant photosynthesis, such as nutrient limitation (Blyth et al., 2021). Whilst Kou-Giesbrecht et al. (2023) reported that TBMs are capable of reproducing the historical terrestrial C sink with a sufficient level of performance, uncertainties persist. TBMs use different modeling approaches to represent N limitation of photosynthesis and the effect of N availability on leaf N, which can lead to varying results regarding plant productivity (Medlyn et al., 2015). Leaf N can be obtained directly from soil N availability by using a fixed parameter or with flexible parametrization using leaf C: N ratios (Thomas et al., 2015). Increasing model complexity regarding modeling the N limitation can thereby also introduce further uncertainties into the estimates of the carbon sink (Fisher and Koven, 2020; Famiglietti et al., 2021), through both process and parameter uncertainty, given the inclusion of new process equations. These uncertainties are also reflected in significant divergence of N pools and fluxes modelled by the current generation of TBMs (Kou-Giesbrecht et al., 2023). In addition, the modelled responses of photosynthesis to elevated atmospheric carbon dioxide (CO₂) or to N deposition vary between different TBMs, requiring a better understanding of the N cycle (Davies-Barnard et al., 2020; Arora et al., 2020; Meyerholt et al., 2020; Zaehle et al., 2014). It is therefore important to better constrain the nitrogen dynamics in these models.

One of the major sources of uncertainty in modeling the land carbon sink with TBMs is the uncertainty in estimating the leaf photosynthetic capacity and photosynthetic rate (Bonan et al., 2011; Rogers et al., 2017). Leaf chlorophyll (chl_{leaf}) is intrinsically related to plant photosynthesis, due to its role in generating biochemical energy for the carboxylation reactions within the Calvin–Benson cycle, through the harvesting of solar radiation. Previous work has demonstrated that leaf chlorophyll content is a strong proxy for photosynthetic capacity (Croft et al., 2017; Lu et al., 2020; Luo et al., 2021). The maximum carboxylation rate at the 25 °C reference temperature ($V_{c(max),25}$) represents the limitation of photosynthesis by the Rubisco enzyme, which is the main regulator in light-saturated photosynthesis (Houborg et al.,

2013). Due to the investment of N in chl_{leaf} molecules and an optimal N investment strategy to ensure close co-ordination between light-harvesting and carboxylation reactions, there is a close relationship between leaf N and chl_{leaf} (Sage et al., 1987; Evans, 1989). In-situ observations of chl_{leaf} can therefore be used to improve the parametrization of physiological schemes within TBMs to improve GPP estimates (Luo et al., 2018, 2019; Lu et al., 2022; Thum et al., 2025). However, many of the contemporary TBMs do not represent chl_{leaf}, and the widely used version of the FvCB model (Farquhar et al., 1980) for photosynthesis description does not explicitly take into account the role of chl_{leaf} in photosynthesis. In addition, the majority of TBMs only consider total canopy N and its vertical distribution (Vuichard et al., 2019; Best et al., 2011; Clark et al., 2011).

In addition to in-situ observations, remote sensing (RS) of the Earth's vegetation provides comprehensive data for evaluating TBMs. Leaf nitrogen is difficult to retrieve directly from RS observations (Farella et al., 2022), in comparison to chl_{leaf} which is more feasible to derive remotely (Croft and Chen, 2018), due to the presence of large chlorophyll absorption features in visible wavelengths. The advantage of using remotely sensed chlleaf is its global and seasonal coverage and relatively long time span, compared to in-situ observations. Similarly as in-situ observations, RS chl_{leaf} can be harnessed to improve the modeled photosynthetic processes which include $V_{c(max)}$ (Houborg et al., 2013). For example, Liu et al. (2023) retrieved global daily $V_{c(max)}$ for C3 biomes by using RS chl_{leaf} and RS solar-induced chlorophyll fluorescence. Another advantage of RS chl_{leaf} is that they are linked to space-borne observations of leaf area index (LAI), both retrievable remotely (Croft et al., 2020). This allows the modeled leaf surface area to be evaluated simultaneously with chlleaf.

In this study, we utilized a spatial RS chl_{leaf} product (Croft et al., 2020) to evaluate the chl_{leaf} representation of the TBM QUINCY (QUantifying Interactions between terrestrial Nutrient CYcles and the climate system) (Thum et al., 2019; Caldararu et al., 2020), which has fully prognostic coupled carbon and nitrogen cycles. QUINCY includes an explicit representation of chlleaf and its impact on photosynthesis, and also the photosynthetic parameters $V_{c(max),25}$ and the maximum electron transport rate at 25 °C reference temperature $(J_{\text{max},25})$ are directly determined from leaf nitrogen. We analysed model performance with respect to the temporal and spatial distribution of chl_{leaf} and LAI in different ecosystems globally. We further compared the simulated gross primary production (GPP) with the ground-based measurements from eddy-covariance network stations. To understand model-data mismatch, we used a machine learning approach to analyze how different environmental drivers affect both QUINCY and RS chl_{leaf}. We further investigated whether the observed difference in chl_{leaf} between QUINCY and observations is related to modeled N limitation by examining QUINCY's leaf C: N values. Here we use RS data as a reference for evaluation, though we acknowledge that RS data are also simulated product and have different characteristics than in-situ data. In other words, our evaluation can be understood more as a comparison study between TBM and RS-derived data.

Initial results suggested that the modeled response of chl_{leaf} to leaf N was not realistic, foremost because the original leaf nitrogen scheme in QUINCY does not take into account of the observed relationship between chl_{leaf} and $V_{c(max)}$ (Evans and Clarke, 2019). In order to have a more realistic representation, we formulated an alternative leaf N allocation scheme in QUINCY based on Onoda et al. (2017) and Evans and Clarke (2019), where the $V_{c(max)}$ and chl_{leaf} ratio is taken into account, and compared the additional simulation results with the original leaf N allocation scheme.

The objectives of the study were to determine different methods for using RS chl_{leaf} in model evaluation and how RS chl_{leaf} can benefit modeling of coupled C and N cycles. The research questions addressed in this work are as follows:

- Are the spatial and temporal patterns of global chl_{leaf} in QUINCY and RS similar?
- Is QUINCY's performance in modeling chl_{leaf} related to its ability to produce measured annual GPP?
- What are the main environmental drivers that affect QUINCY chl_{leaf} and RS chl_{leaf}?

2 Materials and methods

In this section, we will first present the study sites and observational data, followed by QUINCY model description and simulation setup. Finally, a machine learning approach to determine $\operatorname{chl}_{\operatorname{leaf}}$ environmental drivers is presented. In this study, $\operatorname{chl}_{\operatorname{leaf}}$ denotes both chlorophyll a and b (chl_{a+b}). All the datasets used in the study are presented in Table S1 in the Supplement.

2.1 Description of the sites

We conducted the analysis using two different site sets. The first set was the Protocol for the Analysis of Land Surface Models (PALS) Land Surface Model Benchmarking Evaluation Project (PLUMBER2) (Ukkola et al., 2022). The second site set, GLOBAL, is based on the study by Caldararu et al. (2022).

PLUMBER2 (Abramowitz et al., 2024) was designed for serving in a model intercomparison project for land surface models, and provides CO₂ eddy covariance measurements and meteorological data for various sites. The time interval of PLUMBER2 site data varies depending on the site, as some of the site data cover only one year, while others cover over a decade. The time span of PLUMBER2 site data is between 1992–2018. Of the available sites, we included 143 PLUMBER sites that had RS chl_{leaf}, RS LAI and QUINCY data available, and that were not reported by Abramowitz

et al. (2024) to have anomalous precipitation input data. The GLOBAL site set represents all major climate zones and global biomes, and the site input data is for the years 1989–2018 based on the CRU JRA dataset (Harris, 2020). In our analysis, we used 279 GLOBAL sites for which QUINCY simulations and RS chl_{leaf} data were available and matched in land cover type (see Sect. 2.2.3).

In total, the combined PLUMBER2 and GLOBAL analysis included 422 sites. The locations of the PLUMBER2 and GLOBAL sites are presented in Fig. S1 in the Supplement. The sites are categorized based on the QUINCY plant functional types (PFTs), and the number of GLOBAL and PLUMBER2 sites in each PFT are listed in Table 1.

2.2 Remote sensing data

2.2.1 Remotely sensed chl_{leaf}

We obtained chl_{leaf} content from the global RS product by Croft et al. (2020). The RS chl_{leaf} is derived from the EN-VISAT MERIS full-resolution reflectance data with a twostage radiative transfer model. The spatial resolution of the global RS chl_{leaf} is 300 m, and the data are processed to a 7d temporal resolution for the years 2003-2011. The chl_{leaf} has been retrieved by first modeling the reflectance spectra at the leaf level using two separate models: the 4-Scale model (Chen and Leblanc, 1997) for forested and spatially clumped ecosystems, and the SAIL model (Verhoef, 1984) for cropland and grassland ecosystems. The chl_{leaf} has been then derived from the leaf reflectance spectra by using the PROSPECT leaf optical model (Jacquemoud and Baret, 1990). The influence of gaps has been partially minimized in the RS chl_{leaf} by Croft et al. (2020) by gap-filling the missing data with the year 2010 data and a smoothing algorithm. A detailed description of the RS chl_{leaf} product is presented in Croft et al. (2020).

In addition, we obtained chlorophyll content data based on the Sentinel-3 OLCI data (Reyes-Muñoz et al., 2022) for two needle-leaved sites for which we also had in-situ chl_{leaf} measurements (see Sect. 2.3.2). The RS chl_{leaf} product by Reyes-Muñoz et al. (2022) is generated by involving Gaussian process regression algorithms, and the training data for the algorithm consisted of simulated top of atmosphere radiance from coupled canopy radiative transfer model SCOPE and the atmospheric radiative transfer model 6SV. The aim was to further evaluate the magnitude and the seasonality of chl_{leaf} for the needle-leaved evergreen boreal forests by using data from a different Earth observation instrument and also obtained with a different retrieval algorithm than with RS chl_{leaf} by Croft et al. (2020).

2.2.2 Remotely sensed LAI

We used the GEOV1 remotely-sensed leaf area index (LAI) product from the Copernicus Global Land Service (Baret

Abbreviation	Long name	Nr of sites, PLUMBER2	Nr of sites, GLOBAL	Nr of sites, all
BNE	Boreal needle-leaved evergreen	20	50	70
TeNE	Temperate needle-leaved evergreen	8	6	14
BNS	Boreal needle-leaved deciduous	0	6	6
TeBE	Temperate broad-leaved evergreen	4	4	8
TeBS	Temperate broad-leaved deciduous	25	20	45
TrBR	Tropical broad-leaved rain deciduous	2	2	4
TrBE	Tropical broad-leaved evergreen	9	38	47
TeC	C3 crops	21	0	21
TeH	C3 grasslands	34	69	103
TrH	C4 grasslands	20	84	104
all	_	143	279	422

Table 1. List of QUINCY PFTs and the corresponding number of sites in the PLUMBER2 and GLOBAL site sets.

et al., 2013), which is the same RS LAI product used to retrieve the RS chl_{leaf} by Croft et al. (2020). GEOV1 LAI is derived from the SPOT-VGT satellite data and has a temporal resolution of ten days and a spatial resolution of 1 km. We used data for the years 2003–2011.

2.2.3 Post-processing of the RS data

As RS chl_{leaf} depends in part on the assumed land cover (LC) type for each grid cell, it was important to ensure that the QUINCY chl_{leaf} values for each site represented the same ecosystems as RS chl_{leaf}. We compared the PFT values used in the QUINCY simulations with the LC values from a European Space Agency Climate Change initiative (ESA-CCI-LC) LC map (ESA, 2017), from which the LC types were also taken for the RS chl_{leaf} retrieval modeling by Croft et al. (2020). A list of LC types is presented in Table S2 in the Supplement, and the LCs associated with each PFT in our comparison are presented in Table S3 in the Supplement. For each site, we first selected the site grid cell and the eight surrounding grid cells, i.e. the 3×3 cell area, from the ESA-CCI LC map. We then checked whether the QUINCY PFT matched the LC type for each of the grid cells, and added to a list those grid cells that had a matching land cover type to the QUINCY PFT. We then picked from the RS chl_{leaf} grid data only those listed grid cells that had a matching land cover type, and calculated an area average RS chl_{leaf} based on the listed cells. This area average was calculated separately for each time step. If there were no matching grid cells in the 3×3 surrounding cells, we extended the search to cover 5×5 surrounding cells, and looped through 25 grid cells. We then selected the matching cells from the 25 cells, and calculated the area average RS chl_{leaf} for each time step. There were eight PLUMBER2 sites and 80 GLOBAL sites for which we did not find any matching grid cells, and these sites were excluded from the analysis. We only used the topof-canopy chl_{leaf} values from QUINCY to ensure that the values were consistent with the RS-based values. In addition, the RS chl_{leaf} for the needle-leaved sites was multiplied by $\frac{\pi}{2}$. This was done to account for the half-hemispherical needle geometry in the remote sensing retrieval (Stenberg et al., 1995).

The RS LAI data were only retrieved using the one grid cell where the site was located, i.e. the PFT classification of a site did not affect the RS LAI post-processing. If no data were available in that particular grid cell, we extended the area to cover $\pm 0.01^{\circ}$ latitude and longitude degrees and used the average of the whole extended area.

2.3 In-situ observations

2.3.1 Eddy covariance flux observations

Ground station GPP observations were available for the PLUMBER2 sites, and the data were taken from the eddy covariance flux tower dataset provided by Ukkola et al. (2022). The dataset includes flux tower data from three data releases: FLUXNET2015 (Pastorello et al., 2020), La Thuile (FLUXNET, 2024), and OzFlux (Isaac et al., 2017). The flux data were gap-filled using statistical methods depending on the length of the gap. The short gaps up to four hours were gap-filled using linear interpolation methods. Gaps that were longer than four hours were gap-filled with linear regression against the incoming shortwave (SW) radiation, air temperature and humidity, or only against the SW radiation if the other two variables were missing. Depending on the site, the flux time series ranged from one to 20 years, between the years 1992 and 2018 (see Ukkola et al., 2022, Table S1). Data from all years were used, and therefore, the GPP time series are not necessarily from the same time interval as RS chl_{leaf}.

2.3.2 chl_{leaf} and leaf C: N in-situ measurements

To further investigate the chl_{leaf} magnitude and seasonal cycle for boreal needle-leaved evergreen (BNE) forests, we performed an additional comparison for RS and QUINCY output with in-situ observations for two PLUMBER2 sites: Sodankylä site (FI-Sod) in Finland (67.4° N, 26.6° E) (Thum

et al., 2007) and Niwot Ridge (US-NR1) in the United States (40.0° N, -105.5° E) (Bowling and Logan, 2019). Both sites are characterized as needle-leaved forest sites with strong seasonal cycle and harsh winters. FI-Sod is classified as boreal forest, and US-NR1 as subalpine, and it is located in a mountainous terrain. The sites were selected as both sites had a time series of chl_{leaf} observations. In addition, there were also fraction of absorbed photosynthetic radiation (fAPAR) in-situ observations available at FI-Sod, which we used in our analysis. Further details about chl_{leaf} data collection and the use of in-situ observations is provided in Sect. S1 in the Supplement.

We also used in-situ observations from the TRY database (Kattge et al., 2011) to compare the in-situ leaf C: N ratios with our model-derived values. The leaf C: N observations were retrieved from the TRY database for two sites: the boreal needle-leaved forest station Hyytiälä in Finland (FI-Hyy, 61.8° N, 24.3° E) and the deciduous forest site, Morgan Monroe State Forest site in the US (US-MMS, 39.3° N, -86.4° E). The FI-Hyy measurements are sampled from Scots pine tree. US-MMS is a secondary successional broadleaved forest, and the leaf C: N measurements cover various different deciduous trees: sugar maple (Acer saccharum), American beech (Fagus grandifolia), American elm (Ulmus americana), Northern red oak (Quercus rubra), and other deciduous species. The sites were selected based on consistent measurement time with the QUINCY simulations, and to expand the geographical gradient of in-situ measurements, and also to include an example of a temperate broad-leaved deciduous forest (TeBS) site.

2.4 Terrestrial biosphere model QUINCY

We used the terrestrial biosphere model QUINCY (Thum et al., 2019; Zaehle et al., 2019), which includes fully coupled carbon, nitrogen and phosphorus (P) cycles, as well as water and energy fluxes in ecosystems. Global vegetation ecosystems are classified into eight categories by PFTs. In addition, there are several acclimation mechanisms that allow a smooth transition of ecosystem functioning in different climatic conditions. Vegetation is represented as an average individual, which is characterised by its height and diameter as well as an average individual density, and which includes structural tissues (leaves, fine roots and fruits, and for trees additionally coarse roots, sapwood and heartwood) as well as two non-structural pools, labile and reserve. The canopy is divided into ten layers. The canopy scheme incorporates photosynthesis and canopy conductance separately for sunlit and shaded leaves for each canopy layer.

Plants in QUINCY respond to soil N availability. This includes a response in leaf N content, which decreases if there is not enough N is available. Leaf nitrogen is divided into structural and photosynthetically active components. The photosynthesis scheme explicitly accounts for the role of chl_{leaf}. Photosynthesis is calculated using the Kull and

Kruijt (1998) model. According to this model, in the light-saturated part of the leaf, photosynthesis is the minimum of electron transport rate-limited photosynthesis (determined by $J_{\text{max},25}$) and the carboxylation capacity-limited photosynthesis (determined by $V_{\text{c(max)},25}$). In the non-light-saturated part, photosynthesis is determined by the electron transport-rate-limited photosynthesis. Chlorophyll partly determines the depth of the light-saturated layer in the leaf. Thus, all the three photosynthetically active components of leaf nitrogen influence the photosynthesis calculation in QUINCY, as described by Friend et al. (2009), Zaehle and Friend (2010), and Thum et al. (2019). The photosynthesis model by Kull and Kruijt (1998) is extended to cover C4 plants (Friend et al., 2009).

The C: N ratios of leaves and fine roots respond dynamically to the balance of C and N in the labile pool. When there is shortage of N supply, the leaf C: N ratio increases and vice versa. The ratios are constrained to an empirically derived range based on the TRY database (Kattge et al., 2011), and the lower and upper boundaries are presented in Table S4 in the Supplement. Soil carbon and nitrogen pools are modeled on the basis of the CENTURY soil model (Parton et al., 1993) and the soil profile is divided into 15 vertical soil layers, extending to a depth of 9.5 m with increasing depth when moving deeper into the ground.

The seasonal development of leaf biomass and LAI depend on the plant's ability to grow new tissues, given the availability of C and N, as well as the fractional allocation to plant organs. This fractional allocation is constrained by allometric relationships and the availability of nutrients and water. Meteorological conditions and soil moisture are used as phenological controls for LAI development, and it is assumed that plant growth is zero outside the growing season. Both the beginning and the end of the growing season, which determine the LAI seasonal cycle, depend partly on the PFT. For cold and temperate deciduous and herbaceous PFTs, the start of the season is described as a function of the accumulated growing degree days. The accumulated growing degree days are calculated from the beginning of the last dormancy period. In addition, for these PFTs, the end of the growing season is triggered when the weekly air temperature falls below a PFT-specific threshold. For PFTs of rain-deciduous phenology, the start of the season is triggered when the soil moisture stress factor exceeds the PFT-specific threshold values. For these PFTs and also for the warm herbaceous PFTs, the trigger for the end of the season is again the soil moisture stress factor. An additional condition for herbaceous PFTs to end their growing season is when the weekly carbon balance, i.e. the residual between GPP and maintenance respiration, becomes negative. The evergreen needle-leaved trees are assumed to be in a continuous growing season. A more detailed description of QUINCY is presented in Thum et al. (2019).

2.4.1 Original leaf nitrogen allocation in QUINCY

QUINCY allocates the total canopy nitrogen to canopy layers with exponentially decreasing N content towards the bottom of the canopy as in Niinemets et al. (1998). At the leaf level, nitrogen is partitioned into structural ($f_{N,struct}$) and photosynthetic fractions at each canopy layer (Friend et al., 1997). The photosynthetic fractions are associated with chlorophyll ($f_{N,chl}$), Rubisco ($f_{N,rub}$), which is used directly to calculate $V_{c(max)}$, and electron transport ($f_{N,et}$), which is used to calculate the maximum rate of electron transport (f_{max}).

The fraction of leaf N in the structural compartment for each layer, $f_{N,struct}$, is calculated as a linear function of leaf N, as presented in Zaehle and Friend (2010):

$$f_{\text{N,struct}} = k_0^{\text{struct}} - k_1^{\text{struct}} \cdot N_{\text{leaf}}$$
 (1)

where k_0^{struct} is the PFT-specific maximum fraction of structural leaf N, and $k_1^{\text{struct}} = 7.14^3 \text{ (g N)}^{-1}$ is the slope of structural leaf N with respect to total N (N_{leaf}) (Friend et al., 1997).

The fraction of leaf N in the chlorophyll compartment, $f_{N,chl}$, is calculated as an increasing function of cumulative LAI across the canopy (LAI_{cum}) (Kull and Kruijt, 1998; Friend et al., 2009; Zaehle and Friend, 2010):

$$f_{\text{N,chl}} = \frac{k_0^{\text{chl}} - k_1^{\text{chl}} e^{-k_{\text{fn}}^{\text{chl}} \cdot \text{LAI}_{\text{cum}}}}{a_n^{\text{chl}}}$$
(2)

where $k_0^{\rm chl}$ and $k_1^{\rm chl}$ are PFT-specific empirical parameters, $k_f^{\rm chl}$ is an empirical parameter describing the increasing $f_{\rm N,chl}$ with canopy depth, and LAI_{cum} is the cumulative LAI. $a_n^{\rm chl} = 25.12\,{\rm mol\,mmol}^{-1}$ describes the molecular N content of chlorophyll (Evans, 1989). The $k_0^{\rm chl}$ and $k_1^{\rm chl}$ parameters are the same for trees and C3 grasslands, but different for C4 grasslands. The rest of the leaf N is divided between the $f_{\rm N,rub}$ and the $f_{\rm N,et}$ with a fixed ratio of 1.97 (Wullschleger, 1993).

2.4.2 Alternative leaf N allocation

In the alternative leaf N allocation scheme, $f_{N,rub}$ is calculated based on a function of leaf mass per area (LMA) as described by Onoda et al. (2017). The formulation using the QUINCY PFT-specific LMA values (Thum et al., 2019) is as follows:

$$f_{\text{N,rub}} = \frac{-21.1 \cdot \log_{10}(\text{LMA}) + 57.5}{100}.$$
 (3)

The fraction in electron transport, $f_{N,et}$, is derived from $f_{N,rub}$ using the fixed ratio of 1.97. $f_{N,chl}$ is then calculated as a function of $f_{N,et}$, based on the results by Evans and Clarke (2019):

$$f_{\text{N,chl}} = \frac{37.3}{8.85 \cdot 2.0} f_{\text{N,et}} e^{-k_n \text{LAI}_{\text{cum}}}$$
 (4)

where $k_n = -0.11$ describes the increase in chl_{leaf} within the canopy depth. The $f_{N,\text{struct}}$ is then calculated as the remaining part of the leaf N, $(f_{N,\text{struct}} = 1 - f_{N,\text{chl}} - f_{N,\text{et}} - f_{N,\text{rub}})$.

2.4.3 QUINCY simulation setup

We conducted individual site-level QUINCY simulations for the PLUMBER2 and GLOBAL sites. In QUINCY, C3 crops and C3 grasslands are grouped as one PFT, i.e. they are simulated with the same parametrization. The current version of QUINCY does not include management practices. Therefore, C3 crops do not differ from C3 grasslands in QUINCY simulations. Similarly, boreal and temperate needle-leaved evergreen forests are grouped into the same PFT. In this study, we labeled those as the needle-leaved evergreen sites with a mean annual temperature below 10 °C as boreal and the rest as temperate.

We ran all the simulations with active C and N cycles, i.e. the CN version of the model. Soil P availability was kept at a level that did not limit plant uptake or soil organic matter decomposition. The model input fields included half-hourly meteorological data: SW and longwave radiation, air temperature, precipitation, surface air pressure, relative humidity and wind speed. In addition, atmospheric CO₂, and N and P deposition rates are part of the input drivers. Model input parameters include PFT classification and various soil properties such as soil texture, bulk density, soil depth, rooting depth and inorganic soil P content. The specific leaf area (SLA), which is the inverse of LMA, is a PFT-specific constant. There is only one PFT associated with each site. The list of PFTs and the corresponding PFT abbreviations are presented in Table 1.

For the PLUMBER2 sites, the meteorological fields were obtained from the PLUMBER2 dataset (Ukkola et al., 2022). Depending on the PLUMBER2 site, meteorological data was available from 1992 to 2018 (Ukkola et al., 2022, Table S1). For the GLOBAL sites, the meteorological data were obtained from the CRU JRA dataset, and covered the years 1989–2018. Soil physical and chemical parameters (bulk density, rooting and soil depth and soil texture) were retrieved from the SoilGrid dataset (Hengl et al., 2017). Atmospheric CO₂ concentrations were retrieved from the Global Carbon Budget 2019 data (Friedlingstein et al., 2019), and the N and P deposition data are based on the dataset presented by Lamarque et al. (2010, 2011).

For each site, we ran a 1000 year model spin-up in order to bring the soil and vegetation biogeochemical pools into quasi-equilibrium. During the spin-up, atmospheric CO₂ concentration, N deposition and P deposition data were used by repeating the values from the period between 1901–1930. Meteorological data were taken from a random year of observed meteorological data. After spin-up, the simulations were conducted as transient simulations, starting from the year 1901. The transient simulation was continued with data from a random year of observed meteorology until the start

of the period for which observed meteorological data were available. For the PLUMBER2 sites, the start of the period was site-dependent, while for the GLOBAL sites, the meteorological data began in 1989. In the transient simulation, atmospheric CO₂ concentrations and N deposition were retrieved for the corresponding years from the data sources mentioned above.

In addition to the simulation with the default QUINCY setup for the PLUMBER2 and GLOBAL sites, we carried out four additional simulations for the PLUMBER2 sites to analyze how N limitation and changes in leaf nitrogen allocation affect the results. First, we performed an additional simulation with the QUINCY C-only setup (QUINCY C_{only}), where only the C cycle was active but the leaf stoichiometry was described with a fixed parametrization. This was done in order to compare the effect of N limitation with the results of the default QUINCY CN-simulation. We then conducted a CNsimulation with the alternative leaf N allocation scheme, as described in Sect. 2.4.2. After that, we ran a CN-simulation using the default QUINCY settings, but modified the source code by multiplying the $f_{N,chl}$ parameter by 1.3. This was done in order to see the effect of increasing fraction of leaf N allocated to chlleaf. Finally, we carried out a simulation with the alternative leaf N allocation, but the $f_{N,rub}$ was multiplied by 1.3, to represent a 30 % increase in the Rubisco fraction, which leads to an increase in the chl_{leaf} fraction. The additional simulations with increased $f_{N,chl}$ and $f_{N,rub}$ were only performed for the TeBS sites in the PLUMBER2 site set. The list of different simulations is presented in Table S5 in the Supplement.

2.5 Feature importance analysis

The impact of different environmental drivers on the simulated and RS chlleaf magnitude was examined using the permutation feature importance algorithm, based on random forest (RF) regression fitting (Breiman, 2001). RF is a regression tree-based machine learning method that is able to capture non-linear correlations. Permutation importance indicates the contribution of an individual input variable to the statistical performance of a model. In other words, permutation importance can be used to investigate the influence of an environmental driver on a target variable, which in our case is chl_{leaf}. In addition, we analyzed the importance of each selected environmental variable via the SHAP (SHapley Additive exPlanations, Lundberg and Lee, 2017) values. We used the SciKit Learn Python3 package for both RF and permutation importance (Pedregosa et al., 2011), and the *shap* Python library by Lundberg and Lee (2017) (https://github.com/shap/shap, last access: 23 June 2025) to compute the SHAP values.

The target data for the RF models were either QUINCY chl_{leaf} or RS chl_{leaf}. We trained 22 separate RF models. Of the 22, the first ten RFs were dedicated to monthly QUINCY chl_{leaf} and each individual PFT from PLUMBER2

and GLOBAL sites. In addition, we trained one RF model with monthly data from all of the sites and QUINCY chl_{leaf}, using both PLUMBER2 and GLOBAL sites. The remaining RF models were used for monthly RS chl_{leaf} and individual PFTs, and one model with data from all of the sites.

The input data consisted of monthly means of air temperature and PAR, and annual sums of precipitation and N deposition, and annual means of Standardized Precipitation Evapotranspiration Index (SPEI) at each of the sites. The input variables for the RF models were selected from the available environmental data that showed the least correlation between each other. Air temperature, precipitation and N deposition were those used as input in the QUINCY simulations. The SPEI data were retrieved from the global drought monitoring dataset by Vicente-Serrano et al. (2023b). We used the SPEI with a two-week time scale (SPEI 0.5 months), which was then averaged as monthly mean data. The spatial resolution of the SPEI dataset was $0.5^{\circ} \times 0.5^{\circ}$, and we chose the same time steps as in the QUINCY data. The PAR radiation was taken from the QUINCY output, and it was converted from SW radiation with the model (Howell et al., 1983).

The random forest hyperparameters were set to default values, but the maximum number of features per node was set to three. A recommended value for the maximum number of features per node in RF regression is one-third of the input features (Hastie et al., 2009), but here we used a slightly higher value in order to maintain representative subset sizes.

First, we tested the performance of RF models by splitting the data using the $train_test_split$ function in SciKit Learn. We used 75% of the data for preliminary training and 25% for preliminary testing. The coefficient of determination (R^2) scores for the preliminary training and preliminary testing phases are reported in Table S6 in the Supplement. Next, we used all the data (i.e. the preliminary training and preliminary testing data) for the final training of the models.

After the final RF model training, we calculated the corresponding permutation feature importance values for each model. The permutation feature importance algorithm was used with 30 repeats ($n_{\text{repeats}} = 30$) and with a fixed random state. Finally, the SHAP values were calculated using data averaged over three months. The higher positive SHAP values indicate a stronger, increasing effect on chl_{leaf}, and the lower negative SHAP values indicate a decreasing effect on chl_{leaf} compared to the average.

2.6 Data-analysis

In this study, the QUINCY chl_{leaf} is the top-of-canopy chl_{leaf}, as mentioned in Sect. 2.2.3. For the PLUMBER2 sites, we used all the available years from the QUINCY simulations, as well as from RS and eddy covariance observations. For the GLOBAL sites, we used QUINCY simulation data for the years in which RS chl_{leaf} data was available for each site.

We calculated the PFT mean chl_{leaf} , LAI 90th percentile for GLOBAL and PLUMBER2 sites for both QUINCY and

RS. In addition, we calculated the PFT mean annual GPP for GLOBAL and PLUMBER2 sites for QUINCY, but only the PFT mean for the GPP ground observations on the PLUMBER2 sites, as no GPP ground station measurements were available for the GLOBAL (artificial) sites. We used the 90th percentile of LAI instead of the mean values. This was done to reduce the effect of differences in seasonal amplitude and timing variation between QUINCY and RS and to focus on LAI values during the growing season. We calculated the Pearson correlation coefficients (r) between QUINCY and RS site-level mean chl_{leaf} , LAI 90th percentile and GPP annual sum values, and the statistical significance of the correlation using Student's t test, with a threshold value of 5 % for the statistical significance.

We analyzed the seasonal cycle of chl_{leaf} and LAI for the PLUMBER2 and GLOBAL Northern Hemisphere (NH) sites separately for different PFTs. In addition, the analysis of the PLUMBER2 sites included GPP. First, we calculated the averaged seasonal cycle over years for each site and variable. Then, using these averaged seasonal cycles, we calculated the mean seasonal cycle per PFT across sites and the standard deviation between sites for each day of year (DOY). This was done for QUINCY simulated values and for RS and eddy covariance CO₂ observations. Using the PFT-averaged seasonal cycles, we calculated the Pearson correlation (*r*) and root mean squared error (RMSE) between QUINCY and the observations.

For the NH PLUMBER2 TeBS sites, we estimated the start of season (SOS), the end of season (EOS) and the length of season (LOS) based on the PFT-averaged chlleaf, LAI and GPP. We calculated the seasonal metrics using the method as described by Thum et al. (2025). The SOS and EOS values from the PFT-averaged GPP were calculated using the first and last pass of the threshold value. The threshold was set at 30 % of the 90th percentile value of the PFT-averaged mean seasonal cycle of GPP. For LAI and chl_{leaf}, the threshold was determined using the difference between the summer and winter values. Winter values were calculated using the mean values from January and February, and summer values were calculated using the mean values from June and July. The threshold was then set to 20 % of the difference, added to the winter mean, (i.e. $y_{\text{thres}} = x_{\text{winter}} + 0.2 \cdot (x_{\text{summer}} - x_{\text{winter}})$). The earliest DOY for SOS was set to 50. LOS was calculated as the difference between EOS and SOS.

We calculated the residuals between the QUINCY chl_{leaf} mean and RS chl_{leaf} for each site, and compared these to the QUINCY leaf C:N ratios. Leaf C:N can be considered as an indicator of N availability for plants. The aim was to examine whether the under- or overestimation of QUINCY chl_{leaf} was related to nitrogen limitation in the model. The comparison was done for BNE, C3 grasslands (TeH) and TeBS. These PFTs were assumed to represent different vegetation types: BNE represents evergreen forests, TeH grasses and TeBS deciduous forests. In addition, we calculated the mean chl_{leaf} interannual variability (IAV) for

the PLUMBER2 and GLOBAL sites. We first calculated the standard deviation of the annual mean chl_{leaf} for each site, and then the average of the standard deviations at the PFT level and over all sites.

We analyzed the seasonal cycle of chl_{leaf} for two evergreen needle-leaved PLUMBER2 sites, FI-Sod and US-NR1 (see Sect. 2.3.2), by comparing the QUINCY simulations, in-situ observations and remote sensing observations. We calculated the averaged seasonal cycles over years for QUINCY and for remote sensing chl_{leaf} and compared them with in-situ observations. Furthermore, we analyzed the seasonal cycles of LAI, fAPAR and GPP for the FI-Sod site and compared the QUINCY simulated values to the observations. We also compared briefly the simulated mean annual averaged leaf C: N values to in-situ observations for two PLUMBER2 sites, FI-Hyy and US-MMS.

3 Results

3.1 Evaluation of simulated chl_{leaf}, LAI and GPP against observations

3.1.1 Yearly values

At the PFT level, QUINCY estimates of the mean annual chl_{leaf} and LAI agree relatively well with the RS-derived chl_{leaf} and LAI values (Figs. 1, S2, and S3 and Tables S7 and S8 in the Supplement) for all PLUMBER2 sites, with correlations of r=0.61 for chl_{leaf} and r=0.51 for LAI (Table S7). QUINCY does overestimate both chl_{leaf} and LAI for temperate broad-leaved evergreen forest (TeBE) and tropical broad-leaved rain deciduous forest (TrBR) sites, with temperate needle-leaved evergreen forest (TeNE) and C3 crops (TeC) also overestimated for LAI on a mean PFT scale. Despite the variability in simulated chl_{leaf} and LAI values in comparison to RS-derived values, the overall simulated GPP for all PLUMBER2 sites correlates well between QUINCY estimates and eddy-covariance data (r=0.71; Table S7 and Fig. S4 in the Supplement).

As expected, the within PFT variability between sites reveals greater scatter, the nature of which differs for chl_{leaf} and LAI (Figs. S2 and S3). For chl_{leaf} in all cases apart from TeBS, tropical broad-leaved evergreen forest (TrBE) and C4 grasslands (TrH), there is a lack of variation in the QUINCY chl_{leaf}, which present more constant values and smaller dynamic range compared to RS chl_{leaf} values (Fig. S2 and Tables S7 and S8). This is particularly pronounced for TeC and TeH sites, which give a range of 10–17 μg cm⁻² for TeC and 4–17 μg cm⁻² for TeH, for QUINCY and a range of 13–46 and 2–47 μg cm⁻² for RS, respectively. The site-level LAI estimates by contrast generally present a larger dynamic range (with the exception of TeBS, TeNE, TeBE and TrBE). The TrH in particular show a large overestimation in QUINCY

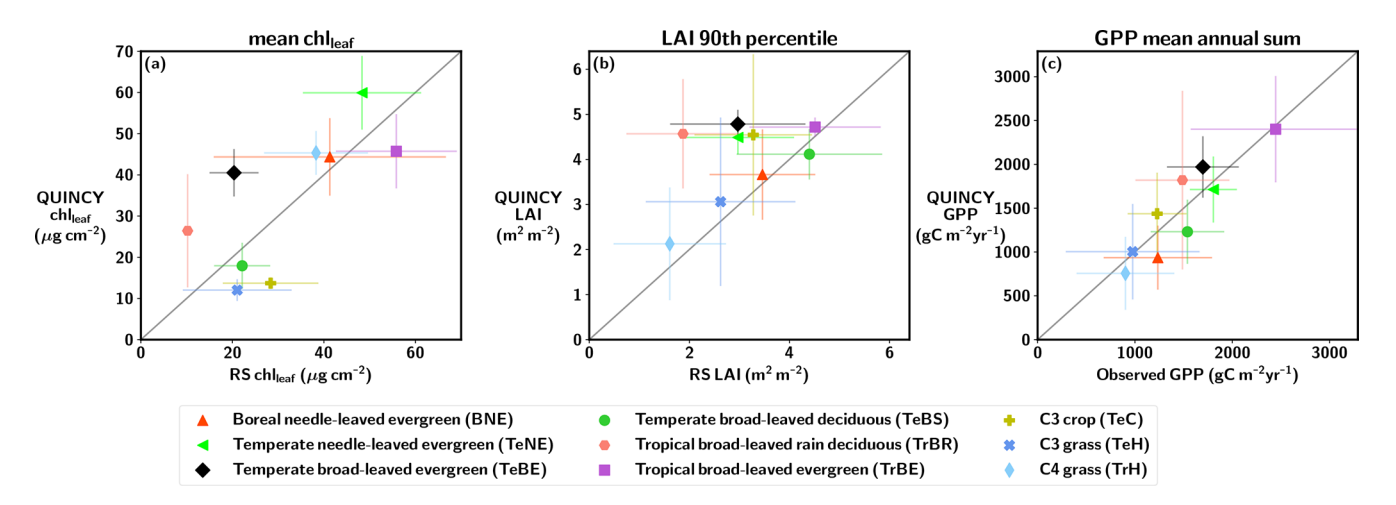


Figure 1. The PFT mean (a) chl_{leaf}, (b) LAI, and (c) GPP for the PLUMBER2 sites. The standard deviation is represented by whisker lines. A 1:1 line is marked with a gray line.

LAI compared to RS LAI at higher LAI values (LAI > 2.5) (Fig. S3).

The site-level GPP results show a good correlation between OUINCY estimates and eddy-covariance observations across PFTs. Whilst the correlation is generally along the 1:1 line, in 58% of the PLUMBER2 sites, OUINCY underestimates the GPP on average by about $400 \,\mathrm{g}\,\mathrm{C}\,\mathrm{m}^{-2}\,\mathrm{yr}^{-1}$. The majority of these underestimations are for BNE and TeBS forests. The QUINCY overestimation of GPP is mainly for crops and grasslands, with an average overestimation of $384\,\mathrm{g}\,\mathrm{C}\,\mathrm{m}^{-2}\,\mathrm{yr}^{-1}$ across $42\,\%$ of the PLUMBER2 sites. For the PLUMBER2 sites, the slight LAI overestimation of the TrH sites does not seem to lead to an overestimation of the mean GPP, but the QUINCY PFT mean GPP $(756 \,\mathrm{g}\,\mathrm{C}\,\mathrm{m}^{-2}\,\mathrm{yr}^{-1})$ is lower than the PFT mean of the observations (902 g C m⁻² yr⁻¹). Due to very high LAI values for the GLOBAL TrH sites, the QUINCY mean GPP for the GLOBAL TrH sites was $1461 \,\mathrm{g}\,\mathrm{C}\,\mathrm{m}^{-2}\,\mathrm{yr}^{-1}$ (not shown), and QUINCY chl_{leaf} mean was $50.2 \,\mu \text{g cm}^{-2}$.

The QUINCY over- or underestimation in chlleaf did not have a strong, detectable geographical pattern when assessed together and separately for all PFTs. The residual chl_{leaf}, i.e. the difference between the mean QUINCY and RS values, is shown in Fig. S5 in the Supplement on a map showing the geographical location of each site. For the C3 grassland sites, the QUINCY mean chlleaf was rather small compared to the RS chl_{leaf}. When analyzing the residuals for the C3 grasslands, the northernmost sites seem to have less negative residuals in magnitude than for the sites around latitudes 30–60° N. This was also the case when the relative residual was analyzed (not shown). The greater QUINCY underestimation of chl_{leaf} for the warmer, southern C3 grassland sites is not related to the GPP underestimation. Interestingly, for the GLOBAL C3 grassland sites the LAI over/underestimation shows an opposite pattern to QUINCY chlleaf: the northern sites show more negative LAI residual, and sites around latitudes 30–60° N mostly QUINCY overestimation of LAI (not shown), which could be due to the fact that RS chl_{leaf} is calculated using RS LAI.

The mean IAV of RS chl_{leaf} over all PFTs is $4.11\pm3.18\,\mu g\,cm^{-2}$, which is much higher than the corresponding value for QUINCY $(1.35\pm1.52\,\mu g\,cm^{-2})$. The RS chl_{leaf} IAV is higher for all other PFTs except for TrH, where the QUINCY chl_{leaf} IAV was $3.39\pm2.04\,\mu g\,cm^{-2}$, and the RS chl_{leaf} IAV was $3.37\pm2.35\,\mu g\,cm^{-2}$. The largest differences in IAVs between RS and QUINCY were seen for the evergreen sites. For example, the RS chl_{leaf} IAV for the BNE sites is 5.95 ± 3.51 , and the QUINCY chl_{leaf} IAV is $0.5\pm0.4\,\mu g\,cm^{-2}$.

3.1.2 Seasonal cycle

The annual cycle of chlleaf for the PLUMBER2 NH TeBS sites (Fig. 2) is similar when comparing QUINCY and RS. However, the start of the growing season is delayed in QUINCY. The SOS, EOS and LOS values for the PFTaveraged PLUMBER2 NH TeBS sites are presented in Table S9 in the Supplement. The QUINCY SOS for LAI is approximately 13 d later in spring compared to the RS LAI. Similarly, the end of the growing season is delayed in QUINCY, and the EOS of QUINCY chlleaf occurs approximately 10 d later than in RS chl_{leaf}. While the RS LAI shows a decrease throughout the autumn season, QUINCY LAI remains at a high value until day of year (DOY) 280, which corresponds to mid-October. The EOS for QUINCY LAI is approximately 30 d later than for RS LAI. However, senescence occurs more rapidly in QUINCY than in the observations.

Figure 2c shows that the GPP between DOY 90–150 for QUINCY is slightly lower than in the observations. The spring development of GPP is slower in QUINCY than in the observations, though the QUINCY SOS of GPP occurs almost at the same time as in the measurements. Although the simulated LAI remains at the summer level until DOY \sim 280, the simulated GPP decreases due to the environmental conditions in autumn. However, the delay in autumn LAI senescence is reflected in the OUINCY GPP EOS, which is approximately 26 d later than for the GPP observations. The delay in the QUINCY spring GPP is compensated partly for by the delayed end of the season where the QUINCY GPP is higher than the observed GPP after DOY 275. The mean GPP 3 month sum for the PLUMBER2 NH TeBS sites for spring (March, April and May, MAM) is 289 g C m⁻² for the observations, while for QUINCY, the value is $196 \,\mathrm{g\,C\,m^{-2}}$. The corresponding 3 month sum values for autumn (September, October, November, SON) for observations is 256, and $351 \,\mathrm{g}\,\mathrm{C}\,\mathrm{m}^{-2}$ for QUINCY.

Figures S6 and S7 in the Supplement show the PFT-mean seasonal cycles of chl_{leaf} and LAI for the PLUMBER2 and GLOBAL NH sites, and Fig. S8 in the Supplement for GPP for the PLUMBER2 NH sites. The most visible difference between QUINCY and RS chl_{leaf} and LAI seasonality can be observed for the boreal and temperate evergreen sites (Figs. S6a, c, and f and S7a, c, and f): QUINCY shows very little variation across seasons, while the RS indicates more variation throughout the year with a clear seasonal cycle. Nevertheless, the QUINCY GPP for these PFTs (Fig. S8a, b, and e) shows a similar annual cycle as the eddy covariance observations, and the correlation r for the evergreen needleleaved sites is high (r > 0.95). For the boreal needle-leaved deciduous forest (BNS) sites (Figs. S6b and S7b), the biases in seasonal cycle were similar to the TeBS results (Figs. S6d and S7d).

QUINCY chl_{leaf} for TeH and TeC sites show a delay in spring compared to RS chl_{leaf}, but this was not observed for QUINCY LAI. In autumn, the decrease in QUINCY chl_{leaf} and LAI occur later than in RS. For the TrH sites (Fig. S6j), the seasonal cycle of QUINCY chl_{leaf} and LAI differ from the observed seasonal cycle. The lowest PFT mean chl_{leaf} for QUINCY is in April (DOY ~ 100). Of the 47 TrH sites in the NH, 74 % of the sites had a higher QUINCY winter (December, January, February, DJF) chl_{leaf} average compared to the QUINCY spring (March, April, May, MAM) chl_{leaf} mean. Furthermore, 55 % of the TrH NH sites were such that the QUINCY DJF means of both chl_{leaf} and LAI were higher than the QUINCY MAM means. RS chl_{leaf} shows (Fig. S6j) the largest TrH averages for summer (June, July, August, JJA) and September, and a fairly clear seasonal cycle.

3.1.3 In-situ comparison of chl_{leaf} for two needle-leaved forests

The seasonal cycle of chl_{leaf}, LAI, fAPAR and GPP for Sodankylä is shown in Fig. 3, and the chl_{leaf} values of the US-NR1 site are presented in Fig. S9 in the Supplement. The mean annual and seasonal chl_{leaf} and GPP values are presented in Table S10 in the Supplement.

Figure 3a highlights that the QUINCY chl_{leaf} values are in a range comparable to the in-situ observations for FI-Sod, but the QUINCY mean (Table S10) is lower than the annual mean of the in-situ measurements. On the contrary, the RS chl_{leaf} by Croft et al. (2020) shows much lower values. In addition, the mean of the Sentinel-3 RS chl_{leaf} is also lower than the in-situ or QUINCY chl_{leaf} but close to the mean RS chl_{leaf} by Croft et al. (2020).

The RS LAI in Fig. 3b shows a clear seasonal pattern for FI-Sod, which has a small effect on the RS chl_{leaf}. The summer (JJA) average RS chl_{leaf} is approximately 10% higher than the winter (DJF) average, which is a relatively small difference compared to the interannual variability (~ 4 μg cm⁻²). In addition, the late spring RS chl_{leaf} between DOY 100–151 show lower values than winter or summer. The late spring RS chl_{leaf} averages 14.6 μg cm⁻², approximately 27% less than the JJA average. Similar spring decreases in RS chl_{leaf} were also observed for other BNE sites. The Sentinel-3 chl_{leaf} peaks in midsummer, and also shows a clear seasonal pattern. The in-situ chl_{leaf} is slightly higher in late summer (DOY 200–240) compared to spring and fall.

QUINCY LAI shows a small seasonal variation, which is reflected in the simulated chl_{leaf}. The winter QUINCY average is slightly lower than the summer QUINCY average chl_{leaf}. The in-situ fAPAR values are in agreement with the simulations during most of the year, but show a stronger seasonal variation than the QUINCY fAPAR (Fig. 3c), with higher values during winter.

QUINCY GPP is in line with the observations until DOY 175, but then decreases until the end of the season (Fig. 3d). However, the difference in annual GPP is not large, and annual QUINCY GPP is on average approximately 9% lower than the in-situ GPP. The difference between observed and simulated GPP after DOY 175 could be due to missing late fall chl_{leaf} development or due to too strong response to a drought.

The mean in-situ chl_{leaf} for the US-NR1 site was close to the QUINCY chl_{leaf} mean (Fig. S9 and Table S10). The minimum value of individual tree samples was 26.8 μg cm⁻² and the maximum was $60.8 \, \mu g$ cm⁻², i.e. there was variation between individual samples that is partially minimized by the averaging. The in-situ observations show a slight increase during spring, but the variation is large due to the small number of samples. The mean in-situ chl_{leaf} for DOY 1–150 is $37.1 \pm 6.1 \, \mu g$ cm⁻², while the mean for summertime is $43.2 \pm 2.3 \, \mu g$ cm⁻². The summer QUINCY chl_{leaf} was close to the annual mean, i.e. there was no pronounced

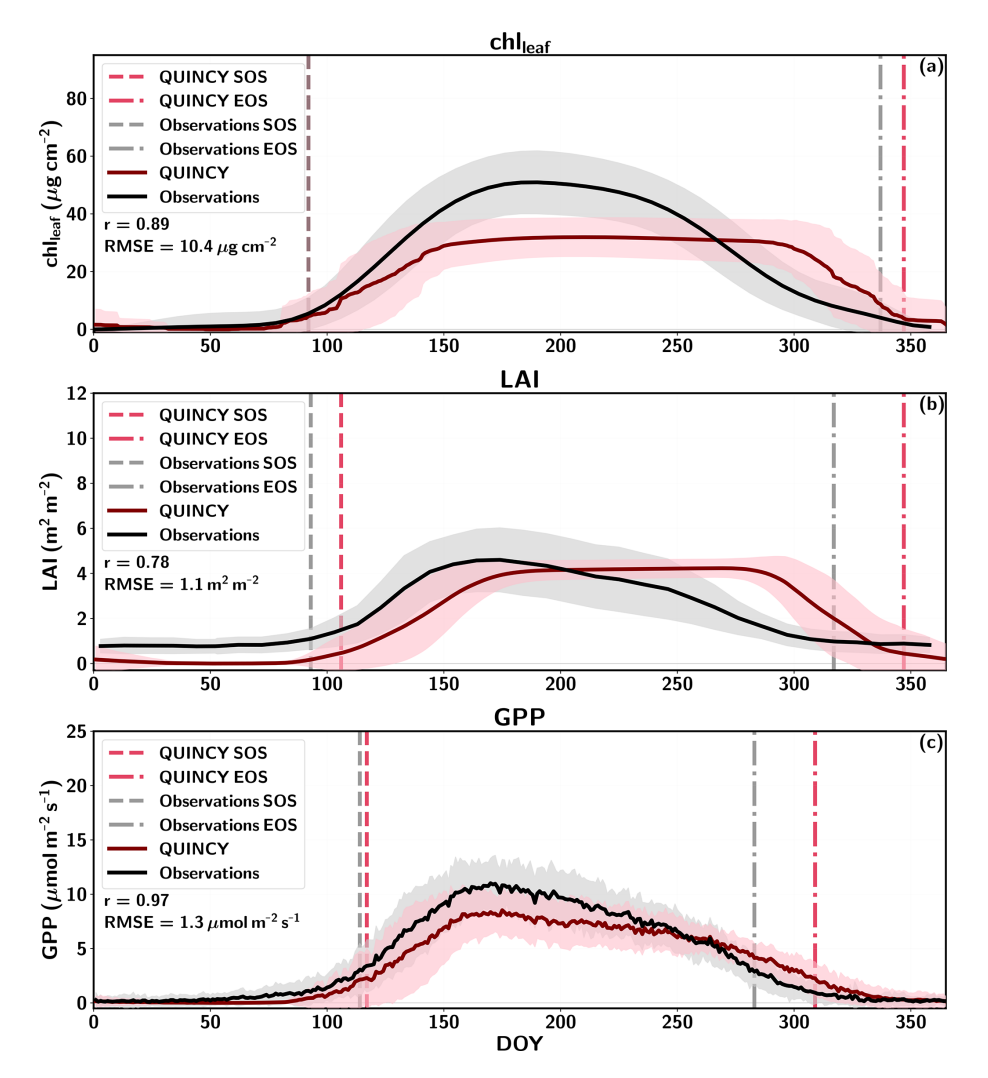


Figure 2. The average annual cycle of (a) chl_{leaf}, (b) LAI, and (c) GPP for the PLUMBER2 TeBS NH sites, as a function of the day of year (DOY). The shaded regions represent the standard deviation between sites. The start of season (SOS) and end of season (EOS) are marked with red (QUINCY) and grey (observations) vertical lines. The Pearson correlation (r) and root mean squared error (RMSE) are marked for each variable.

seasonal cycle. The RS chl_{leaf} annual mean by Croft et al. (2020) was lower than the annual mean chl_{leaf} of in-situ measurements or QUINCY. Interestingly, the RS chl_{leaf} shows a lower JJA mean than the annual mean. Similarly to the FI-Sod RS chl_{leaf}, there is a decrease in the spring chl_{leaf} after DOY 100, and the decrease is more pronounced than for Sodankylä. The minimum value ($\sim 16 \, \mu g \, cm^{-2}$) of RS chl_{leaf} averaged annual cycle appears around DOY 155, with an increase after that. For the Sentinel-3 chl_{leaf}, the mean chlleaf was close to the QUINCY values, although the numerical range was much wider. The JJA mean for Sentinel-3 is close to the in-situ observations, and approximately 32 % higher than the QUINCY JJA chlleaf. The annual QUINCY GPP was 45 % lower than the observed GPP. In addition, the QUINCY JJA LAI (not shown) was $2.2 \pm 0.1 \,\mathrm{m}^2 \,\mathrm{m}^{-2}$, and was lower than the RS JJA LAI $(2.5 \pm 0.2 \,\mathrm{m}^2\,\mathrm{m}^{-2})$, which may partially explain the underestimation of GPP. Bowling et al. (2018) report that the observed in-situ LAI at the site is $3.8-4.2 \,\mathrm{m}^2\,\mathrm{m}^{-2}$.

3.2 Nitrogen limitations in QUINCY

Figures 4a–c show the QUINCY leaf C: N ratios and the corresponding QUINCY chl_{leaf} values for three PFTs. The TeBS sites show an almost linear relationship between chl_{leaf} and leaf C: N with a correlation of r=-0.87 ($p<1\times10^{-13}$). Higher leaf C: N values indicate lower leaf N levels relative to leaf C. This leads to lower chl_{leaf} since chl_{leaf} is a function of leaf N. The same nearly linear relationship between QUINCY leaf C: N and decreasing chl_{leaf} is seen for the BNE sites (Fig. 4c) with a correlation of r=-0.96 ($p<1\times10^{-40}$). The TeH sites represent a more scattered pattern and the correlation is only r=-0.58 ($p<1\times10^{-9}$),

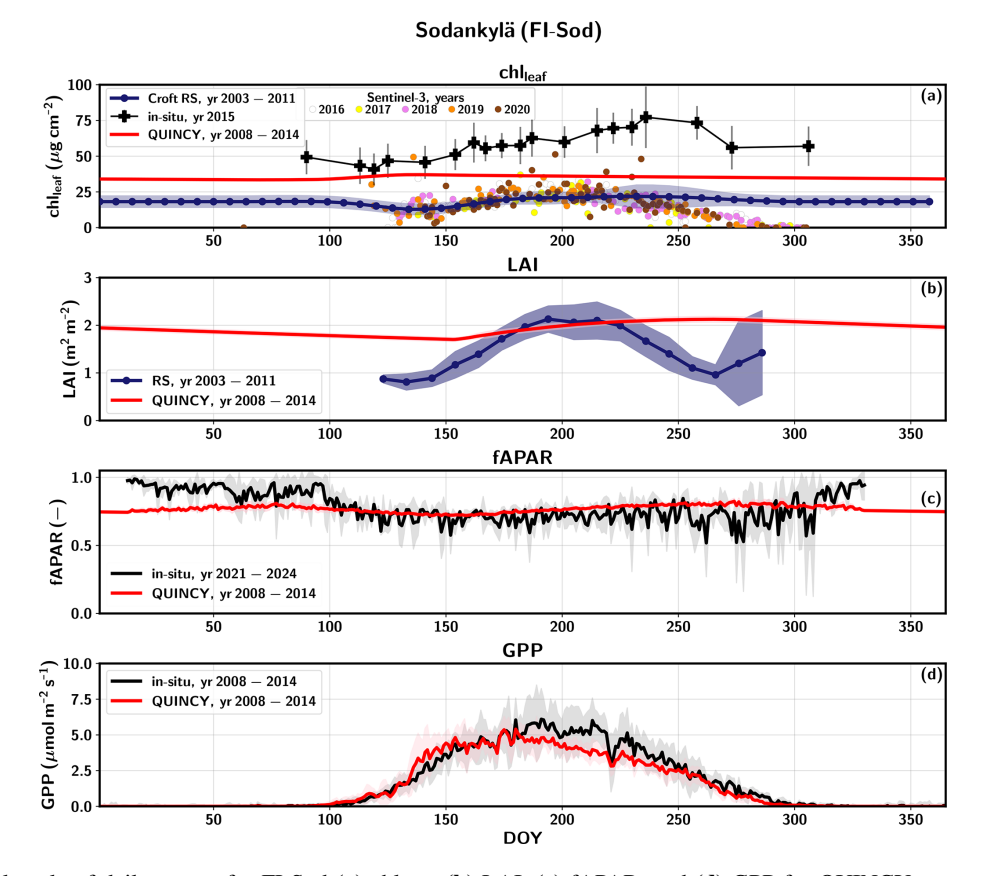


Figure 3. Seasonal cycle of daily means for FI-Sod (a) chl_{leaf} , (b) LAI, (c) fAPAR, and (d) GPP for QUINCY, remote sensing (RS) and in-situ measurements. The standard deviation for some of the data series is visualized as a shaded area. The Sentinel-3 chl_{leaf} values for different years are shown with different colors (2016 = white, 2017 = yellow, 2018 = pink, 2019 = orange, 2020 = brown).

indicating that chl_{leaf} is more influenced by other factors, such as water availability, temperature and precipitation than leaf C:N levels, compared to BNE and TeBS. However, for the TeH sites, both the QUINCY chl_{leaf} and leaf C:N values are in a narrower range compared to the other two PFTs, which partly affects the comparison.

For the TeBS sites, the chl_{leaf} residual is moderately connected to QUINCY leaf C:N values (Fig. 4d), but the same is not true for the BNE and TeH sites. Especially for the PLUMBER2 TeBS sites, the chl_{leaf} residual is more negative for the sites with higher leaf C:N values. The TeH sites do not show much variation in the leaf C:N values, and the chl_{leaf} residual does not appear to be connected to the magnitude of leaf C:N. The 90th percentile of TeH leaf C:N is 35.0, which is 88 % of the QUINCY maximum leaf C:N. The BNE 90th percentile leaf C:N is 51.1 (78 % of the maximum) and the TeBS 90th percentile leaf C:N is 28.1 (73 % of the maximum value).

The majority of the GLOBAL BNE sites are clustered in a region with mean QUINCY chl_{leaf} around 35–40 $\mu g cm^{-2}$ and leaf C: N ratio around 50. The GLOBAL set contains more BNE sites at higher latitudes than the PLUMBER2 set (see Fig. S1). In addition, most (over 83%) of the

PLUMBER2 and GLOBAL sites with leaf C: N \sim 50 are in a region with a mean annual temperature below 5 °C. The median chl_{leaf} residual for the GLOBAL and PLUMBER2 sites is 9.9 μ g cm⁻² and 7.4 μ g cm⁻², respectively.

We analyzed whether the chl_{leaf} residual is connected to the GPP residual, i.e. the difference between QUINCY annual GPP and observed annual GPP (not shown). For the PLUMBER2 TeBS sites, the largest negative GPP residual, i.e. the model underestimated GPP, was for those sites that are more N-limited in QUINCY and have a negative chl_{leaf} residual. For the PLUMBER2 TeH sites, the GPP residual was weakly negatively correlated with the chl_{leaf} residual: the largest positive GPP residual is observed for the sites that have strong negative chl_{leaf} residual. Similarly, the GPP residual for the PLUMBER2 BNE sites was not strongly connected with the chl_{leaf} residual.

We also compared the QUINCY leaf C: N ratios with insitu measured values for two sites (FI-Hyy and US-MMS) obtained from the TRY database. This was done to assess whether the QUINCY leaf C: N values are at a realistic level for individual sites. US-MMS is classified as a TeBS site and FI-Hyy is classified as a BNE site. For the US-MMS site, the QUINCY average leaf C: N was 17.3, and the TRY database

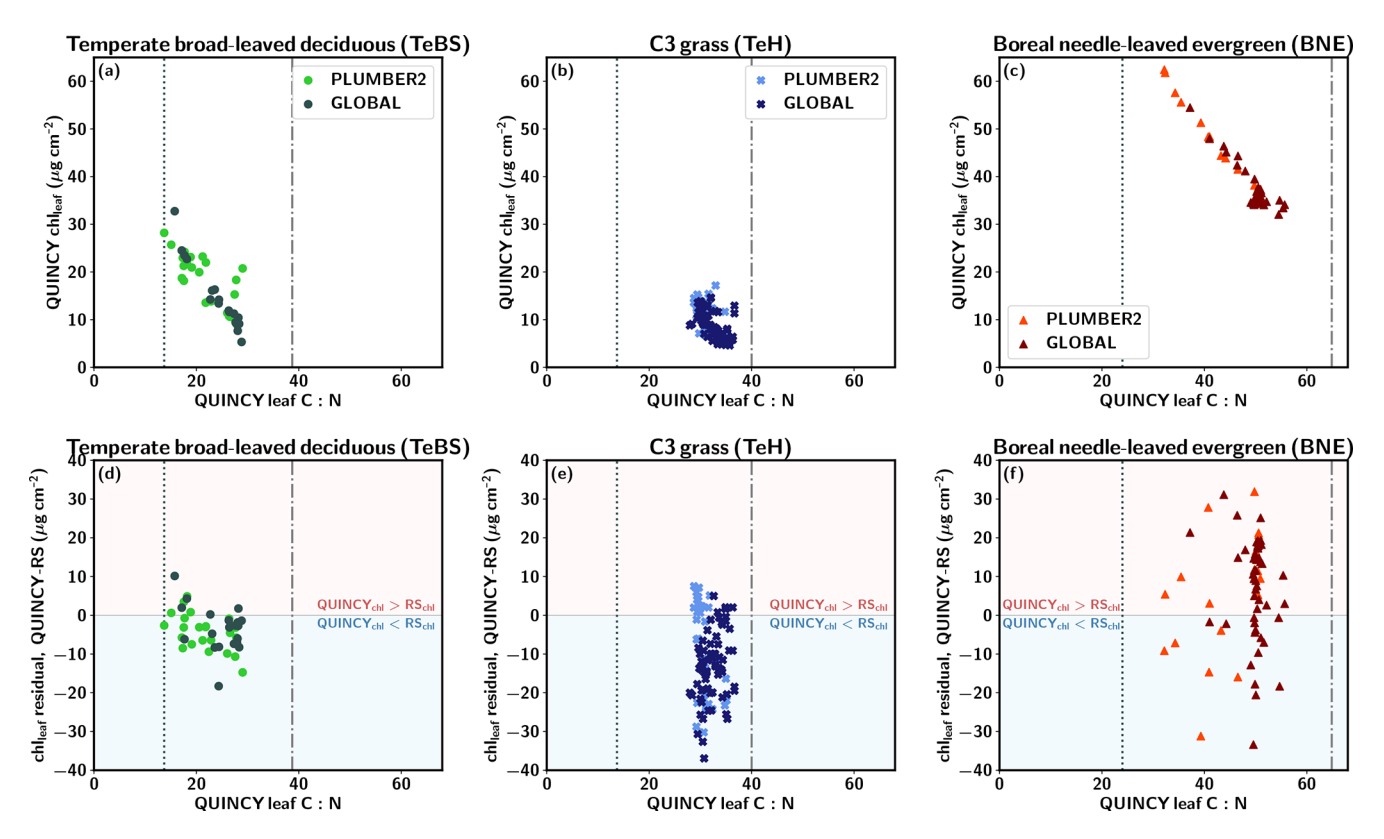


Figure 4. QUINCY leaf C: N and chl_{leaf} and the corresponding residual for (a, d) temperate broad-leaved deciduous (TeBS), (b, e) C3 grassland (TeH), and (c, f) boreal needle-leaved sites (BNE). The vertical lines show the QUINCY leaf C: N minimum and maximum limits.

average was 21.3. The US-MMS QUINCY leaf C: N is close to the lower leaf C: N threshold, and the QUINCY chl_{leaf} is underestimated by 27 % compared to RS chl_{leaf}. For the FI-Hyy site, the values were 46.5 and 38.8, respectively. The QUINCY chl_{leaf} was underestimated by 28 %, which indicates that for FI-Hyy, there is a slightly too strong N-deficit modelled.

In order to study the effects of N limitation, we briefly analyzed the QUINCY C_{only} simulation results for the PLUMBER2 BNE sites (not shown). The results revealed that at low chl_{leaf} values, the difference between GPP from QUINCY default, i.e. CN, and C_{only} simulations was greater than at higher chl_{leaf} levels for the BNE. In addition, for the sites where the N deposition was low, the chl_{leaf} values were also small.

3.3 Leaf N allocation schemes

Figure 5 shows that the alternative, more realistic N allocation scheme leads, on average, to greater chl_{leaf} and GPP underestimation for the TeBS sites compared to the QUINCY default. Furthermore, the alternative N allocation scheme produces lower leaf chl_{leaf} (14.9 \pm 4.4 μ g cm $^{-2}$) than the QUINCY default (17.9 \pm 5.6 μ g cm $^{-2}$) for the PLUMBER2 TeBS sites (Fig. S10 and Table S11 in the Supplement). The corresponding RS chl_{leaf} mean is 22.1 \pm 6.1 μ g cm $^{-2}$. Simi-

larly, the TeBS mean GPP is lower for the alternative N fraction scheme, $1044\pm311~{\rm g\,C\,m^{-2}\,yr^{-1}}$, while the QUINCY default mean GPP is $1231\pm366~{\rm g\,C\,m^{-2}\,yr^{-1}}$. For the observations, the mean GPP is $1539\pm377~{\rm g\,C\,m^{-2}\,yr^{-1}}$. The LAI 90th percentile values are in a similar range ($\sim4\pm1~{\rm m^2\,m^{-2}}$) between the QUINCY default simulation and QUINCY alternative N allocation. The underestimation of GPP and chl_{leaf} is most likely due to lower $f_{\rm N,rub}$. While the summer (JJA) $f_{\rm N,rub}$ for the QUINCY default is on average 0.20 for the PLUMBER2 TeBS sites, the corresponding average for the alternative N allocation scheme is 0.09.

The results for the other PFTs were similar to those for TeBS: the chl_{leaf} and GPP magnitudes were lower with the alternative N allocation scheme (Table S11). An exception is the TrH sites, where the annual GPP was higher with the alternative N allocation than with the default QUINCY scheme. This was due to increased proportions of leaf N in Rubisco and electron transport, while $f_{N,chl}$ was decreased and the $f_{N,struct}$ slightly increased. The PFT mean values for $f_{N,struct}$ and other fractions were calculated over sites globally, i.e. including the Southern Hemisphere sites. This affects the comparison slightly, as the seasonal cycles differ between the Northern and Southern Hemispheres.

Increasing chl_{leaf} affects more the QUINCY default chl_{leaf} levels than QUINCY alternative N fraction output, but the

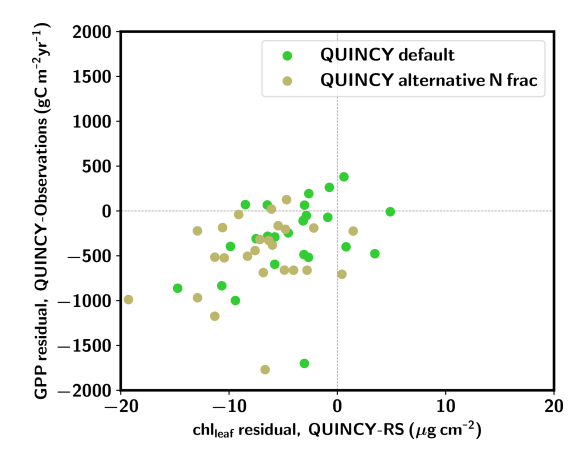


Figure 5. GPP residual (QUINCY – observations) vs. chl_{leaf} residual (QUINCY – observations) for the PLUMBER2 TeBS sites. The QUINCY default scheme results are marked with green circles, and QUINCY alternative N fraction results are marked with beige circles.

difference is not large (Table S12 in the Supplement). When $f_{N,chl}$ is increased in QUINCY default, the mean chl_{leaf} increases by 37.4 %, while the mean LAI 90th percentile decreases by 2.4% and the mean annual GPP decreases by 6.3 %. This is due to the fact that in the QUINCY default, increasing $f_{N,chl}$ decreases leaf N allocated in electron transport and Rubisco, since their fractions of leaf N are calculated after $f_{N,chl}$ (see Sect. 2.4.1). For the alternative N fraction simulations, increasing $f_{N,rub}$ which leads to increase in $f_{N,chl}$ results in different dynamics compared to the QUINCY default scheme. In the alternative N allocation scheme, increasing $f_{N,\text{rub}}$ resulted in an almost linear response in the chl_{leaf} magnitude, with an increase of 24.2 %. The increases in LAI and GPP were more moderate: 5.3 % and 12.1 %, respectively. In the QUINCY default simulation, increasing $f_{N,chl}$ resulted in decreased GPP, while in the alternative N allocation scheme, GPP increased. Furthermore, the fraction in the structural part $f_{N,struct}$ decreases in the alternative N allocation scheme when the $f_{N,rub}$ and, consequently, $f_{N,chl}$ are increased. In the default QUINCY simulation, increasing $f_{N,chl}$ does not directly affect $f_{N,struct}$, but rather indirectly through its influence on leaf N, resulting in only a minor decrease of $f_{N,struct}$.

3.4 The environmental drivers of chlleaf

Figures 6 and S11 in the Supplement show that when the RF fitting is done over all PFTs, the feature importances are very similar between QUINCY and RS. Air temperature has the largest impact on the random forest fitting of both QUINCY chl_{leaf} and RS chl_{leaf}, when the fitting is done using data from all PFTs. The effect of air temperature is even larger for the TeH and TeBS sites compared to the importance calculated over all PFTs. This result is logical, since chl_{leaf} is formed from leaf N, which is partly dependent on tempera-

ture via soil N mineralisation and biological nitrogen fixation (BNF). The QUINCY BNE sites do not show such a strong dependence on air temperature because the evergreen needle chl_{leaf} does not vary as much throughout the year as deciduous chl_{leaf}. However, temperature shows a permutation importance of 0.26 ± 0.003 for QUINCY BNE, which is most likely a result of different sites being in different temperature regimes.

Figure S11 shows that nitrogen deposition is the most dominant driver for evergreen ecosystems for QUINCY chlleaf. For the BNE and TeNE sites, the permutation importance values are 0.95 ± 0.007 and 1.78 ± 0.054 , respectively, and the contribution of other environmental drivers is smaller. For the RS chl_{leaf} of BNE sites, N deposition has the highest permutation importance value (0.84 \pm 0.012), but the role of N deposition in the RS observations is not as pronounced compared to other variables as in QUINCY. The RS chl_{leaf} for the TeNE sites is largely driven by temperature (permutation importance = 0.63 ± 0.043). The grasslands (TeH and TrH) show similar contributions from different variables for QUINCY and RS, although RS chl_{leaf} is less affected by temperature than QUINCY. There is a difference in the permutation importances for the TeC sites between QUINCY and RS, as QUINCY chl_{leaf} is more influenced by temperature and RS chlleaf indicates a slightly mixed effect of different environmental drivers.

The results of the SHAP analysis (Figs. S12 and S13 in the Supplement) are similar to the permutation importance calculations: air temperature is a dominant driver for both QUINCY and RS. In addition, the SHAP values indicate that warmer temperatures lead to higher than average chl_{leaf} values, and colder temperatures lead to lower than average chl_{leaf} values. The SHAP analysis for QUINCY chl_{leaf} suggests that the higher PAR values lead to lower chl_{leaf} values, although the majority of the data points are close to SHAP values of zero, i.e. PAR is not a strong driver of chl_{leaf}, a similar pattern is not found, but the higher PAR would have an increasing effect on chl_{leaf}.

4 Discussion

4.1 QUINCY's ability to reproduce chl_{leaf}, LAI and GPP magnitudes

4.1.1 Magnitude of chl_{leaf}

When analyzed across all sites, QUINCY chl_{leaf} correlated well with RS observations and the PFT specific values were generally in line with the observations, and the simulated PFT-mean values were similar to RS chl_{leaf}. In particular, the PFT mean chl_{leaf} of the BNE and TeBS sites was close to the mean RS observations of these PFTs. However, QUINCY generally produced lower variability in chl_{leaf} between sites

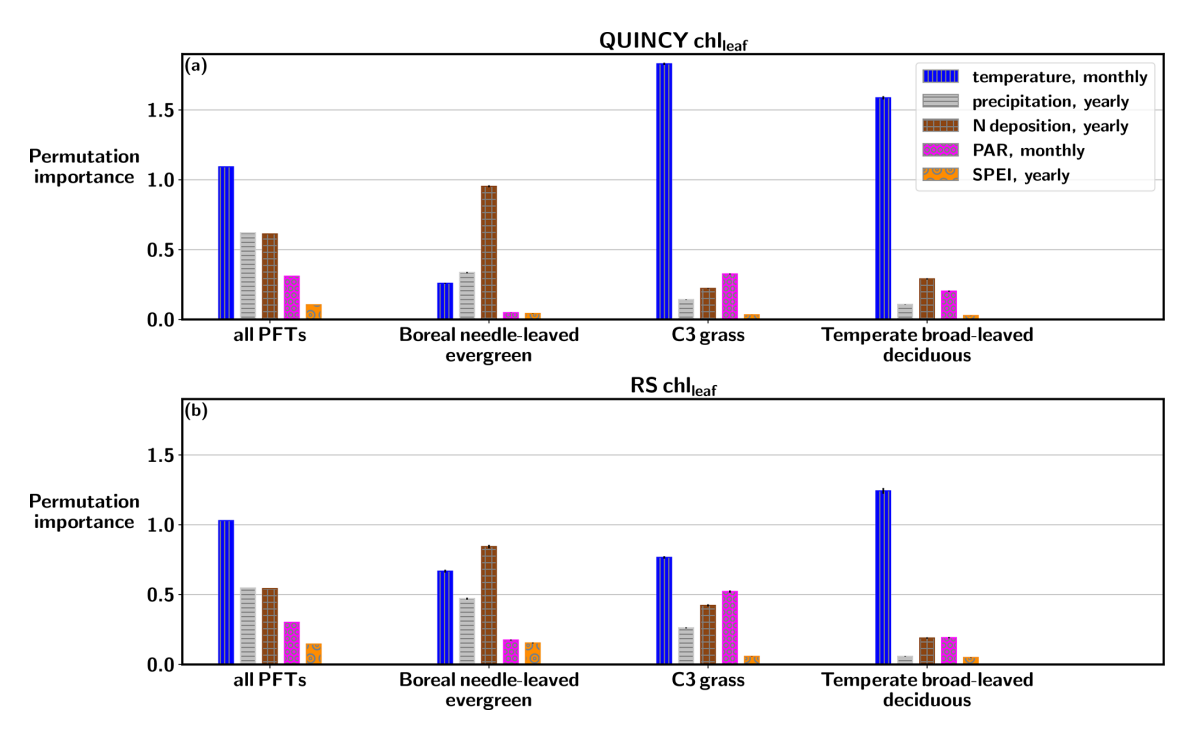


Figure 6. Permutation importance values based on random forest regression fitting for (a) QUINCY chl_{leaf} and (b) RS chl_{leaf}, based on data from all sites, and separately for BNE, TeH, and TeBS sites.

compared to RS. Particularly for C3 grasslands and crops, the QUINCY chl_{leaf} was restricted to too narrow a range compared to RS observations. This suggests that QUINCY lacks some processes that cause variation in RS chl_{leaf} values, and that the QUINCY dynamics for C3 grasses and crops require further in-depth analysis to explain the missing variation. In addition, the chlleaf QUINCY parameterization for C3 grasslands is the same as for trees, which could affect chleaf dynamics. Fertilization and other management practices are not included in the version of QUINCY used in this study, which could explain the difference in the chl_{leaf} numerical ranges between QUINCY and RS. This may affect the comparison of magnitude and seasonality for C3 cropland sites. Lu et al. (2020) gathered a collection of different chl_{leaf} in-situ observations distributed globally. When comparing the QUINCY chl_{leaf} values with those reported by Lu et al. (2020), it was observed that C3 crops and C3 grasslands are most likely underestimated, similarly when compared to the RS chl_{leaf} values. The correlation between QUINCY chlleaf and RS chlleaf was poor for C3 grasslands and C3 crops. This also highlights the need for tuning the QUINCY parameterization for grasslands, and possibly other changes to the model structure to capture the grassland chl_{leaf} dynamics.

Some of the PLUMBER2 sites are located in fens and wetlands, and these are classified as C3 grasslands in QUINCY. The model version of QUINCY used in this study does not include wetlands or fens, and therefore for some of the sites (e.g. FI-Lom in high latitude region) QUINCY does not model the relevant water table depth dynamics, which may influence the carbon and water dynamics at the sites.

For C4 plants, the range for QUINCY values was similar to RS chl_{leaf} for higher values, but lower chl_{leaf} concentrations were missing in QUINCY. Lu et al. (2020) reported 15–60 μ g cm⁻², while the QUINCY chl_{leaf} range for C4 grasslands was 31–72 μ g cm⁻². The RS chl_{leaf} range for C4 grasslands was 12–63 μ g cm⁻². However, it should be noted that QUINCY chl_{leaf} values only represent the top of the canopy, while in-situ observations may have mixed results from different canopy heights, which may affect the comparison.

For the BNE sites, the QUINCY chl_{leaf} overestimation was higher for GLOBAL than PLUMBER sites, and relatively higher portion of GLOBAL BNE sites were located in high latitudes. This suggests that the QUINCY chl_{leaf} overestimation or RS chl_{leaf} underestimation, is more pronounced for the needle-leaved sites in cold regions, which could partly reflect the challenges of optical remote sensing in high latitudes.

Our machine learning-based analysis indicated that QUINCY is able to capture the influence of environmental drivers of the chl_{leaf} in a big picture. QUINCY chl_{leaf} for evergreen sites was driven by N deposition, with other environmental variables contributing less. The same was true for the RS chl_{leaf} for BNE and TrBE but not for TeNE. Additional comparison of QUINCY simulations with active C and N cycles with a C_{only} simulation also demonstrated a similar conclusion. Though, the RS chl_{leaf} for BNE sites seemed to be more temperature-driven than for QUINCY. This could be

explained by differences in the seasonal cycle, as RS chl_{leaf} shows a seasonal pattern for BNE sites, while QUINCY does not. In addition, it was observed that QUINCY chl_{leaf} for the TeC sites was mainly driven by temperature, while RS chl_{leaf} had more equal contributions from different variables. In addition, the footprint size of RS chl_{leaf} may affect the comparison, as crops are typically located in a heterogeneous landscape. The analysis with the SHAP values revealed that higher PAR values could produce lower chl_{leaf} in QUINCY simulations. The decreasing effect of higher PAR values on QUINCY chl_{leaf} could be partly due to the tropical regions, where the PAR radiation does not vary as much throughout the year. The decreasing effect could be also attributed to differences between different sites.

4.1.2 Magnitudes of LAI and GPP

The QUINCY annual GPP showed a good correlation with PLUMBER2 observations, however, the values were underestimated at most of the sites. This could be partly due to a slightly delayed growing season for the deciduous forests (Fig. S8), which hinders the early spring carbon sequestration. The delayed seasonal development calls for tuning the QUINCY phenology parameters, which could benefit the simulations with a reasonable amount of work. However, for some of the PFTs (TeC, TrBR, TeBE), QUINCY overestimated GPP.

The simulated LAI over all PFTs was generally in an agreement with RS LAI (Fig. S3d and Table S8). However, a clear future development point for QUINCY is the overestimation of LAI values, which was the case for most of the PFTs. The overestimation of LAI in QUINCY could be due to, for instance, missing herbivores and management. These effects are currently under development in QUINCY. The overestimation of LAI is pronounced for the C4 grasslands, for which the LAI values in QUINCY were unrealistically high. The very high LAI values were observed for the GLOBAL sites located on the African and South American continents, for which we did not have GPP ground station data. However, the QUINCY GPP for the PLUMBER2 C4 grassland sites was within a reasonable range, and the QUINCY PFT mean GPP was close to the observed PFT mean GPP. This suggests that despite high LAI, QUINCY is able to account for environmental conditions affecting GPP and maintain realistic GPP levels. However, for the GLOBAL C4 grassland (TrH) sites, it was observed that if the simulated extremely high LAI values were coupled with high chl_{leaf}, this resulted in high simulated GPP values. The RS observations could potentially be used in model tuning to balance the overestimation of both LAI and chl_{leaf}.

Although QUINCY tended to overestimate LAI in general, for TeBS it was mostly underestimated. Similarly, the QUINCY mean chl_{leaf} is underestimated at the majority of the TeBS sites. However, when analyzing the residuals for individual sites, the GPP under- or overestimation was not

always related to the chl_{leaf} or LAI residual. Less than half of the 25 PLUMBER2 TeBS sites showed an underestimation for all chl_{leaf}, LAI, and GPP. Overestimation of LAI can potentially lead to too strong shading, which could result in reduced GPP in lower canopy layers. The radiative transfer model might therefore play a role in the underestimated GPP.

4.2 QUINCY's ability to reproduce the observed seasonal cycle

The seasonality of GPP for QUINCY was consistent with the observations for many of the PFTs. However, the seasonality for chl_{leaf} and LAI in QUINCY was found to have differences compared to RS values for some of the PFTs.

The annual cycle of QUINCY chlleaf for deciduous forest sites was similar when QUINCY and RS chlleaf were compared. However, the increase in QUINCY chlleaf in spring occurred late compared to RS chlleaf, as well as decrease in autumn chl_{leaf}. The QUINCY LAI estimations showed similar biases when compared against RS results. However, this was not reflected as prominently in the seasonality of GPP compared to the delay in LAI, most likely due to environmental drivers. This indicates that QUINCY is able to maintain reasonable GPP levels in autumn even when LAI is overestimated. For the NH PLUMBER2 TeBS sites, the PFT-averaged seasonal cycle showed that the QUINCY underestimation of annual GPP is not too strongly affected by the delay in start of the growing season. The GPP sum for the spring (MAM) was underestimated by QUINCY by $\sim 93 \,\mathrm{g}\,\mathrm{C}\,\mathrm{m}^{-2}$, while the overestimation in the autumn (SON) was $95 \,\mathrm{g}\,\mathrm{C}\,\mathrm{m}^{-2}$, i.e. they compensate each other.

The QUINCY chlleaf and LAI seasonality differed from RS observations for the boreal and temperate evergreen sites. QUINCY chlleaf and LAI do not change as much from season to season at these evergreen sites, whereas RS chlleaf and LAI show more variation during the year. The RS chl_{leaf} for BNE forests implied a stronger seasonal cycle than what was seen from in-situ observations at two BNE sites, which was most likely driven by too strong LAI seasonality of the RS product. In addition, the RS observations for the Sodankylä (FI-Sod) and Niwot Ridge (US-NR1) sites indicated a slight decrease in spring chl_{leaf}, and this was seen also for other BNE sites. The decrease in RS chl_{leaf} in spring could be driven by resorption of N to form new needles, or by the impact of the understory during the snow-melt season. A study by Zhang et al. (2019), conducted in a laboratory environment, demonstrated a similar decrease for a boreal evergreen forest. The RS chl_{leaf} retrieval algorithm does not consider variations in understory, and therefore the understory vegetation can cause artifacts to the retrieved needle-leaf reflectance signal. In addition, the mountainous landscape surrounding US-NR1 might affect RS retrieval, which also can create artifacts to the mean RS chl_{leaf}. The Sentinel-3 chl_{leaf} shows the strongest seasonal cycle at the US-NR1 site compared to other products used in this study, which could be partly due to assumptions made in the retrieval processing. For instance, the assumptions made for the LAI seasonality and the effect of snow cover can affect the RS chl_{leaf} retrieval. For temperate broad-leaved evergreen sites, QUINCY did not simulate seasonal variation in chl_{leaf}, while RS chl_{leaf} showed a clear increase in spring and decrease in fall. Site-level studies have indicated contradicting results for chl_{leaf} seasonal cycle for temperate evergreen forests (Joshi et al., 2024; Yasumura and Ishida, 2011), therefore it is not straightforward judge whether the model behavior is erroneous.

The in-situ observations in the boreal Sodankylä forest (Fig. 3a) for the year 2015 showed that the chl_{leaf} concentrations increased throughout the growing season in needle-leaved forests. Similar behavior at other evergreen needle-leaved forests was reported by Laitinen et al. (2000) and Katahata et al. (2007). The increase in chl_{leaf} could indicate that the Sodankylä forest may be N-limited, and requires strong N uptake throughout the summer. The observations from the Niwot Ridge forest did not show such a strong pattern (Fig. S9), as also shown by Bowling et al. (2018), potentially reflecting a different N status of the ecosystem.

For TeC and TeH sites, the seasonal cycle of QUINCY chl_{leaf} was delayed compared to RS, but the bias was not large. The lower QUINCY spring chl_{leaf} for NH TrH sites suggests that the phenological cycle for these sites needs further tuning in QUINCY, and is most likely linked to simulated LAI biases. In QUINCY, the start of senescence is controlled by soil moisture and temperature thresholds. Given the high species diversity in herbaceous systems, both within and between sites, ecosystem-level models such as QUINCY often struggle to capture phenological variation. This is partially due to PFT-level parameters not reflecting diversity at the site level, and partially due to the difficulty of capturing an average response of diverse species.

4.3 Modeling the N cycle and N limitation

QUINCY is one of the state-of-the art TBMs that include an advanced representation of chl_{leaf} in the canopy, and also the connection between chl_{leaf} and N limitation. This allows the intercomparison to remote sensing chl_{leaf} products, which can be further extended to cover analysing the N limitation on photosynthesis and the implications on carbon sequestration efficiency. In addition, our analysis demonstrated how to use chl_{leaf} as a metric to support analysing the N limitation in simulations. However, one needs to keep in mind that the modelled and remotely sensed chl_{leaf} are not completely equivalent, but there are conceptual differences in spatial coverage, for instance.

The strongest QUINCY GPP underestimation for the PLUMBER2 TeBS sites was connected to stronger N-limitation and QUINCY chl_{leaf} underestimation, suggesting a too strong modeled N limitation for these sites. However, the leaf C: N values were not close to the maximum leaf C: N values for the TeBS sites, suggesting that the QUINCY

maximum threshold value of leaf C: N may be slightly too high (Fig. 4d). Though, we compared QUINCY leaf C: N values to the TRY database observation leaf C: N values for two sites, and the QUINCY values were in line with the observations.

Some of the QUINCY chlleaf underestimation for the TeBS sites could be due to lower N availability or allocation to leaves (Fig. 4d). Both the QUINCY underestimation of chlleaf and also GPP could be partly related to modeling deficiencies in the N cycle. The QUINCY mean symbiotic BNF was $\sim 0.3 \,\mathrm{g}\,\mathrm{Nm}^{-2}\mathrm{yr}^{-1}$ for the TeBS sites. Davies-Barnard and Friedlingstein (2020) report that for deciduous broadleaved forests, including both tropical and temperate forests, the mean symbiotic BNF is approximately $0.8 \,\mathrm{g}\,\mathrm{Nm}^{-2}\mathrm{yr}^{-1}$, suggesting that QUINCY symbiotic BNF is underestimated for the TeBS sites. Though, the negative residual of chlleaf between model and observations was higher with the higher leaf C: N values, indicating that QUINCY's modeled N deficit for the TeBS sites is too strong. The analysis shows that for the TeBS forests, the chlleaf residual between simulated and RS chl_{leaf} brings additional information in pinpointing that the N-deficit influence is overestimated at certain sites and contributing to too low GPP.

For the BNE sites, QUINCY overestimated chl_{leaf} compared to RS chl_{leaf}, and the BNE chl_{leaf} and GPP residuals were not correlating, which may be partly be due to RS chl_{leaf} magnitude issues as presented in Sect. 3.1.3. The observed GPP increased as a function of observed chl_{leaf} (not shown), and this was also evident in the simulations. A comparison of QUINCY CN- and C-only simulations for the BNE sites indicated that QUINCY simulates an N deficit at low chleaf values, as GPP was lower with the CN-simulation. Including the N cycle in the simulations improved the model behavior and led to a decrease in simulated chl_{leaf} values at the lower end of the observations and improved model behavior in terms of chl_{leaf} and GPP. This shows a realistic behavior of the QUINCY N cycle. Furthermore, the low chl_{leaf} values coincided with the low N deposition values, indicating that N deposition plays a significant role in the N deficit of these ecosystems, as also shown in the feature importance analysis results.

In addition, the TeH leaf C: N values (Fig. 4e) were closer to the upper bound and covering only approximately half of the leaf C: N range derived from the TRY database, even when we had sites globally distributed across different climatological regions. This suggests that many of the TeH sites are more N-limited in QUINCY compared to BNE and TeBS sites, and that QUINCY has difficulty capturing TeH sites with high leaf N values. This may be a partial cause of the too low and also too static chl_{leaf} values for the TeH sites. For the TeH sites, QUINCY had the largest overestimation of GPP when the modeled chl_{leaf} is the most underestimated. This indicates that the leaf N allocation in QUINCY for TeH sites requires further parameter tuning. The QUINCY dynamics related to N cycling may require further analysis to estimate

the contributions of N deposition and BNF to leaf N content, and to determine whether they are in the range of estimates presented in the reference literature.

Our analysis using the more advanced N allocation routine shows that the chl_{leaf} and GPP magnitudes for the TeBS sites were not improved compared to the observation data. This was partly due to lower $f_{N,rub}$. In the alternative N scheme, $f_{N,chl}$ is a function of $f_{N,et}$ and therefore a function of $f_{N,rub}$, and therefore the lower $f_{N,rub}$ affects both GPP and chl_{leaf} . The underestimation of $f_{N,rub}$ could be partly due to the LMA representation in QUINCY. LMA is the inverse of SLA, and thus it is the same fixed value per PFT, which may be too general a representation with respect to the N allocation scheme. On the other hand, the advanced N allocation scheme provided a more realistic mechanism when $f_{N,\text{rub}}$ was increased by resulting in simultaneous increases in $f_{N,chl}$ and GPP. This indicates that what the alternative N allocation scheme produces is more in line with the current ecophysiological understanding from the literature (Onoda et al., 2017; Evans and Clarke, 2019) regarding the relationship between $V_{c(max)}$ and chl_{leaf}: increasing leaf N in chl_{leaf} does not decrease other photosynthetic fractions, but rather the structural part ($f_{N,struct}$).

4.4 Limitations of the analysis

4.4.1 Limitations due to remote sensing products

Although the satellite product by Croft et al. (2020) agrees well with the in-situ observations (Croft et al., 2020), the satellite retrieval products contain a certain degree of uncertainty. As Boegh et al. (2013) conclude, satellite inversions are often ill-posed inversion problems, which can complicate the retrieval of chl_{leaf} and LAI from remote sensing data. Furthermore, the coverage of the MERIS satellite data is not optimal for certain regions such as South America, the tropics, western Australia, and parts of the boreal zone. This is partly due to gaps in the original data caused by clouds, sensor errors, or light conditions (Tum et al., 2016), though the RS chl_{leaf} product by Croft et al. (2020) is gap-filled with a smoothing algorithm. In addition, in this study, the impact of gaps has been partially reduced by using the average of all years.

Our analysis relied primarily on one RS chl_{leaf} product. For example, RS observations from the Sentinel-3 satellite could be included as they were tested for two sites in this study, although the time periods of the modeled values did not match these observations. The challenge with Sentinel-3 is that the in-situ observations are often provided years back in time, and Sentinel-3 has only been operational since 2016. A potential candidate for combination with Sentinel-based chl_{leaf} products could be Integrated Carbon Observation System (ICOS) observations. The European ICOS research infrastructure provides up-to-date flux measurements

that are also harmonized in terms of measurement and postprocessing techniques.

The remote sensing products of LAI are known to have an overly pronounced seasonal cycle in the boreal needleleaved forests, with LAI values being underestimated in winter, early spring and late fall (Heiskanen et al., 2012; Wang et al., 2019). This is caused by snow and cloud contamination, the understory effects, seasonal variation in needle greenness, low solar zenith angle and poor illumination (Heiskanen et al., 2012; Fang et al., 2013; Wang et al., 2019). In our study, we observed that for the Sodankylä BNE forest, RS LAI showed a clear seasonal pattern, while QUINCY LAI was almost constant throughout the season. We also compared QUINCY fAPAR with in-situ measurements, and this comparison revealed that QUINCY fAPAR followed the in-situ measurements outside the winter season. The in-situ measurements during the winter season were influenced by the low elevation angles of the sun, which limit the reliability of the measurements throughout the winter months and, in mid-winter, result in polar night. Additionally, in spring, ground-level sensors may be covered by snow, compromising data quality even when light conditions would otherwise be sufficient. In addition, as Wang et al. (2024) show, RSbased data often contain inaccuracies in autumn phenology. In our analysis, we used ground-based flux tower observations, which helped to form a comprehensive view of model performance. Croft et al. (2020) report that the RS chl_{leaf} for the needle-leaved forests could benefit from intra-PFT variability in the structural parameters (e.g. canopy height, stem density), which would improve the spatial variability in chl_{leaf}. The contemporary RS products are advancing in this front, providing opportunities to improve other RS products. However, the Sentinel-3 product used in this study was not yet free of these problems.

4.4.2 Limitations due to ground-based observations

The flux tower measurements used in this study were not evenly distributed geographically, but rather concentrated in central Europe and the United States. For example, the number of sites in Central and South America was small, limiting the comprehensiveness of the analysis of the GPP magnitudes relative to ground observations. TBMs and RS products cover larger spatial areas, allowing a global assessment even in areas where the in-situ observations are sparse. In this study, we were able to first analyze data at sites where we had ground station measurements (PLUMBER2), and then extend to other regions without in-situ observations (GLOBAL).

In addition, our analysis does not take into account the potential footprint mismatch between RS chl_{leaf} and the flux towers at the ground stations. Furthermore, the flux tower footprints are not always homogeneous, but represent a mixture of e.g. shrubs and trees. Our QUINCY modeling scheme assumed only one PFT for each of the sites, which may lead

to differences in the GPP if the flux tower is surrounded by heterogeneous plant cover. For some sites, we increased the footprint area of the RS chl_{leaf} to include pixels with the same land cover classification. This increase may have resulted in greater differences in the footprint compared to the flux tower footprint. Site location, topography, and landscape heterogeneity influence the measured CO₂ fluxes (Giannico et al., 2018; Griebel et al., 2016).

4.4.3 Limitations of QUINCY and data-analysis

QUINCY simulations are based on the assumption of an average individual plant or a tree, and do not consider plants of different ages. Similarly, RS inversion algorithms do not consider variations in, for instance, tree height or crown width. As previous studies have shown, chl_{leaf} and nitrogen concentrations in leaves can vary between trees of different ages and also between individuals (Laitinen et al., 2000; Sallas et al., 2003; Warren and Adams, 2001; Thurner et al., 2025). In addition, a PFT can be a very broad category and different tree species may have different characteristics, which is not taken into account in our PFT-based modeling scheme and parameterization. Furthermore, the modeling framework does not account for competition among plants.

Land cover classification can introduce an additional source of uncertainty in this study. There are two sources of uncertainty in the use of land cover maps, as they can be caused by the classification into land cover classes based on spectral reflectance or by the conversion of these land cover classes into the PFT classes that we used (Georgievski and Hagemann, 2019). We have partially accounted for this uncertainty by increasing the number of points that we used for each of the study sites.

The SHAP value analysis with RF fitting resulted in differing results between QUINCY and RS chl_{leaf} and the impact of PAR values on chl_{leaf}. Since the SHAP values only describe the machine learning interpretation of the variable relationships, further investigation of the effect of high PAR values on QUINCY chl_{leaf} would require additional QUINCY simulations where the radiation input fields are increased, but keeping the rest of the input variables the same.

Our analysis could also benefit from including local measurements of in-situ greenness indices (Linkosalmi et al., 2016) to further validate the seasonal cycle of chl_{leaf} for different PFTs, or up-scaled leaf trait maps (Dechant et al., 2024). For instance, the up-scaled maps could provide regional, PFT-specific SLA values that could improve the results of the alternative N allocation scheme.

4.5 Future directions

One objective of this study was to estimate the gain of using RS chl_{leaf} to improve the modeled carbon and nitrogen cycle. However, the approach in this study is based on only one TBM. Though, our analysis included a comparison of

two different chl_{leaf} formulations within a model, which has the advantage that the comparison is not masked out by differences in dynamics between the two models. As recommended by Meyerholt et al. (2020), a model ensemble would provide more robust results, as there is some uncertainty in a single process model approach. However, this would be possible only if other TBMs were to provide chl_{leaf} as a diagnostic, which would also allow that chl_{leaf} could potentially be incorporated into TBM benchmarking platforms, such as ILAMB (Collier et al., 2018).

Another future prospect could be to integrate QUINCY into a digital framework that integrates RS observational time series, TBMs and a radiative transfer model. Based on a comprehensive literature review, Kooistra et al. (2024) propose that such a digital twin combination with data assimilation could enable an almost near-real-time representation of ecosystems and help to overcome the current modeling limitations.

5 Conclusions

The evaluation revealed that the magnitudes of QUINCY chl_{leaf} correlate well with RS chl_{leaf} when analyzed across all plant functional types. However, for some of the PFTs, the QUINCY chlleaf values showed less site-to-site variation compared to the observations. This suggests that the QUINCY parameterization requires further adjustments. RS chlleaf for needle-leaved sites was clearly lower than for QUINCY. The comparison to in-situ chl_{leaf} measurements indicated that RS chl_{leaf} is underestimated for the boreal coniferous forests, while QUINCY chlleaf was in a reasonable magnitude. The inter-comparison of QUINCY and RS chl_{leaf} and LAI seasonal cycles showed that QUINCY produced delayed seasonal pattern for deciduous tress. This suggests that the phenological parameters of QUINCY need further adjustment. In addition, for evergreen needle-leaved forests, there was a clear seasonal pattern in RS chlleaf and LAI, while QUINCY LAI and chlleaf did not vary much throughout the annual cycle. However, the comparison to in-situ chl_{leaf} demonstrated that the RS chl_{leaf} overestimates seasonality of chl_{leaf} for needle-leaved evergreen forests in cold environments, which is likely caused by the RS LAI biases (Heiskanen et al., 2012; Wang et al., 2019) known to happen in these regions. Our analysis highlighted that while QUINCY was able to produce chl_{leaf} magnitudes in the big picture, the representation of chl_{leaf} in QUINCY calls for further improvement. In addition, the results from machine learning-based regression indicated that QUINCY and RS chl_{leaf} have similar contributions from different environmental drivers when the analysis was performed over all sites and PFTs.

We also tested an alternative leaf N allocation scheme, which resulted in more realistic ecophysiological behaviour. A follow-up study with adjusting the parameterization to have a better match with observations, and a larger sample

of sites would provide valuable insights into the benefits of using the alternative N allocation scheme.

Our results reveal that adding chl_{leaf} to the model evaluation provides additional information on photosynthetic processes and leaf N distribution compared to using LAI alone. While LAI provides information about seasonality, information based on chl_{leaf} complements this by enabling us to address the N status of the leaves and identify the main drivers of the chl_{leaf} content. In this paper, we have demonstrated the applicability of using remotely sensed chl_{leaf} as an evaluation point for TBMs. Our study highlights the potential of the use of RS chl_{leaf} as a model evaluation tool for analysing the C and N cycles.

Code and data availability. The QUINCY model codes are available under a GPL v3 license. The scientific code of QUINCY relies on software infrastructure from the MPI-ESM environment, which is subject to the MPI-M License Agreement in its most recent form (https://www.bgc-jena.mpg.de/en/bsi/projects/quincy/ software, last access: 3 June 2025). The source code is available online https://doi.org/10.17871/quincy-model-2019 (Zaehle et al., 2019), release 76b2549 (last access: 3 June 2025), but access is limited to registered users. Readers interested in running the model should request a username and password via the Git repository. Model users are strongly encouraged to follow the fair-use policy (https://www.bgc-jena.mpg.de/en/bsi/projects/ quincy/software, last access: 3 June 2025). The QUINCY simulated data used in this study are available at https://doi.org/10.57707/fmib2share.f8ab5f4ed6534b1597a2db73cc5175ff (Miinalainen, 2025) (last access: 6 October 2025). The forcing data to run the QUINCY model are stored in the model repository.

The global drought monitoring SPEI data is available in https://global-drought-crops.csic.es/#map_name=all_spei_0.5# map_position=2211 (last access: 3 June 2025) (Vicente-Serrano et al., 2023a).

The post-processed RS chlleaf (Croft al., 2020) the PLUMBER2 and **GLOBAL** for https://doi.org/10.57707/fmisites is available at b2share.f8ab5f4ed6534b1597a2db73cc5175ff (Miinalainen, 2025) (last access: 6 October 2025).

The Sodankylä chl_{leaf} in-situ measurement data is available in https://doi.org/10.5281/zenodo.17192030 (Peltoniemi et al., 2025) (last access: 24 September 2025).

The Sodankylä fAPAR measurement data is available at https://doi.org/10.57707/fmi-b2share.f8ab5f4ed6534b1597a2db73cc5175ff (Miinalainen, 2025) (last access: 6 October 2025).

The Sentinel3 RS chl_{leaf} can be retrieved using the scripts available from here: https://github.com/psreyes/S3_TOA_GPR_1 (Reyes-Muñoz and Salinero-Delgado, 2022).

Supplement. The supplement related to this article is available online at https://doi.org/10.5194/bg-22-6937-2025-supplement.

Author contributions. TT, TM, and SZ designed the study. AO and TM wrote scripts for the data analysis. MA collected the Sodankylä fAPAR data. MP provided the Sodankylä leaf chl_{leaf} data. HC provided the remote sensing chl_{leaf} data. TM drafted the manuscript stem. All authors participated in the interpretation of the results and manuscript writing.

Competing interests. The contact author has declared that none of the authors has any competing interests.

Disclaimer. Publisher's note: Copernicus Publications remains neutral with regard to jurisdictional claims made in the text, published maps, institutional affiliations, or any other geographical representation in this paper. While Copernicus Publications makes every effort to include appropriate place names, the final responsibility lies with the authors. Views expressed in the text are those of the authors and do not necessarily reflect the views of the publisher.

Acknowledgements. We acknowledge Erkka Rinne and the Ministry of Transport and Communications through the Integrated Carbon Observing System (ICOS) research and ICOS Finland for the Sodankylä fAPAR in-situ observations. We thank Maiju Linkosalmi for the Sodankylä in-situ chl_{leaf}. We also acknowledge Pablo Reyes-Muñoz for providing the Sentinel-3 OLCI remote sensing chl_{leaf} data for the Sodankylä and Niwot Ridge sites. We thank Gab Abramowitz for the PLUMBER2 data. In addition, the authors thank Gabriela Sophia and Manon Sabot for helping to retrieve data from the TRY database. The authors also thank the QUINCY scientific programmers Jan Engel and Julia Nabel for technical support. For computing resources, we acknowledge Max Planck Institute for Biogeochemistry. We thank two anonymous reviewers whose feedback improved this paper.

Financial support. This research has been supported by the Research Council of Finland (grant nos. 330165, 337552, 359342, and 359196).

The article processing charges for this open-access publication were covered by the Max Planck Society.

Review statement. This paper was edited by Benjamin Stocker and reviewed by two anonymous referees.

References

Abramowitz, G., Ukkola, A., Hobeichi, S., Cranko Page, J., Lipson,
M., De Kauwe, M. G., Green, S., Brenner, C., Frame, J., Nearing, G., Clark, M., Best, M., Anthoni, P., Arduini, G., Boussetta,
S., Caldararu, S., Cho, K., Cuntz, M., Fairbairn, D., Ferguson, C.
R., Kim, H., Kim, Y., Knauer, J., Lawrence, D., Luo, X., Malyshev, S., Nitta, T., Ogee, J., Oleson, K., Ottlé, C., Peylin, P., de
Rosnay, P., Rumbold, H., Su, B., Vuichard, N., Walker, A. P.,

- Wang-Faivre, X., Wang, Y., and Zeng, Y.: On the predictability of turbulent fluxes from land: PLUMBER2 MIP experimental description and preliminary results, Biogeosciences, 21, 5517–5538, https://doi.org/10.5194/bg-21-5517-2024, 2024.
- Arora, V. K., Katavouta, A., Williams, R. G., Jones, C. D., Brovkin, V., Friedlingstein, P., Schwinger, J., Bopp, L., Boucher, O., Cadule, P., Chamberlain, M. A., Christian, J. R., Delire, C., Fisher, R. A., Hajima, T., Ilyina, T., Joetzjer, E., Kawamiya, M., Koven, C. D., Krasting, J. P., Law, R. M., Lawrence, D. M., Lenton, A., Lindsay, K., Pongratz, J., Raddatz, T., Séférian, R., Tachiiri, K., Tjiputra, J. F., Wiltshire, A., Wu, T., and Ziehn, T.: Carbonconcentration and carbon–climate feedbacks in CMIP6 models and their comparison to CMIP5 models, Biogeosciences, 17, 4173–4222, https://doi.org/10.5194/bg-17-4173-2020, 2020.
- Baret, F., Weiss, M., Lacaze, R., Camacho, F., Makhmara, H., Pacholcyzk, P., and Smets, B.: GEOV1: LAI and FAPAR essential climate variables and FCOVER global time series capitalizing over existing products. Part1: Principles of development and production, Remote Sens. Environ., 137, 299–309, https://doi.org/10.1016/j.rse.2012.12.027, 2013.
- Best, M. J., Pryor, M., Clark, D. B., Rooney, G. G., Essery, R. L. H., Ménard, C. B., Edwards, J. M., Hendry, M. A., Porson, A., Gedney, N., Mercado, L. M., Sitch, S., Blyth, E., Boucher, O., Cox, P. M., Grimmond, C. S. B., and Harding, R. J.: The Joint UK Land Environment Simulator (JULES), model description Part 1: Energy and water fluxes, Geosci. Model Dev., 4, 677–699, https://doi.org/10.5194/gmd-4-677-2011, 2011.
- Blyth, E. M., Arora, V. K., Clark, D. B., Dadson, S. J., De Kauwe, M. G., Lawrence, D. M., Melton, J. R., Pongratz, J., Turton, R. H., Yoshimura, K., and Yuan, H.: Advances in land surface modelling, Current Climate Change Reports, 7, 45–71, https://doi.org/10.1007/s40641-021-00171-5, 2021.
- Boegh, E., Houborg, R., Bienkowski, J., Braban, C. F., Dalgaard, T., van Dijk, N., Dragosits, U., Holmes, E., Magliulo, V., Schelde, K., Di Tommasi, P., Vitale, L., Theobald, M. R., Cellier, P., and Sutton, M. A.: Remote sensing of LAI, chlorophyll and leaf nitrogen pools of crop- and grasslands in five European landscapes, Biogeosciences, 10, 6279–6307, https://doi.org/10.5194/bg-10-6279-2013, 2013.
- Bonan, G. B., Lawrence, P. J., Oleson, K. W., Levis, S., Jung, M., Reichstein, M., Lawrence, D. M., and Swenson, S. C.: Improving canopy processes in the Community Land Model version 4 (CLM4) using global flux fields empirically inferred from FLUXNET data, J. Geophys. Res.-Biogeo., 116, https://doi.org/10.1029/2010JG001593, 2011.
- Bowling, D. and Logan, B.: Conifer Needle Pigment Composition, Niwot Ridge, Colorado, USA, 2017–2018, https://doi.org/10.3334/ORNLDAAC/1723, 2019.
- Bowling, D. R., Logan, B. A., Hufkens, K., Aubrecht, D. M., Richardson, A. D., Burns, S. P., Anderegg, W. R., Blanken, P. D., and Eiriksson, D. P.: Limitations to winter and spring photosynthesis of a Rocky Mountain subalpine forest, Agr. Forest Meteorol., 252, 241–255, https://doi.org/10.1016/j.agrformet.2018.01.025, 2018.
- Breiman, L.: Random forests, Mach. Learn., 45, 5–32, https://doi.org/10.1023/A:1010933404324, 2001.
- Caldararu, S., Thum, T., Yu, L., and Zaehle, S.: Whole-plant optimality predicts changes in leaf nitrogen under variable

- CO₂ and nutrient availability, New Phytol., 225, 2331–2346, https://doi.org/10.1111/nph.16327, 2020.
- Caldararu, S., Thum, T., Yu, L., Kern, M., Nair, R., and Zaehle, S.: Long-term ecosystem nitrogen limitation from foliar δ^{15} N data and a land surface model, Glob. Change Biol., 28, 493–508, https://doi.org/10.1111/gcb.15933, 2022.
- Chen, J. and Leblanc, S.: A four-scale bidirectional reflectance model based on canopy architecture, IEEE T. Geosci. Remote, 35, 1316–1337, https://doi.org/10.1109/36.628798, 1997.
- Clark, D. B., Mercado, L. M., Sitch, S., Jones, C. D., Gedney, N., Best, M. J., Pryor, M., Rooney, G. G., Essery, R. L. H., Blyth, E., Boucher, O., Harding, R. J., Huntingford, C., and Cox, P. M.: The Joint UK Land Environment Simulator (JULES), model description Part 2: Carbon fluxes and vegetation dynamics, Geosci. Model Dev., 4, 701–722, https://doi.org/10.5194/gmd-4-701-2011, 2011.
- Collier, N., Hoffman, F. M., Lawrence, D. M., Keppel-Aleks, G., Koven, C. D., Riley, W. J., Mu, M., and Randerson, J. T.: The International Land Model Benchmarking (ILAMB) system: design, theory, and implementation, J. Adv. Model. Earth Sy., 10, 2731–2754, https://doi.org/10.1029/2018MS001354, 2018.
- Croft, H. and Chen, J.: 3.09 Leaf Pigment Content, in: Comprehensive Remote Sensing, edited by: Liang, S., Elsevier, Oxford, https://doi.org/10.1016/B978-0-12-409548-9.10547-0, 117–142, 2018.
- Croft, H., Chen, J. M., Luo, X., Bartlett, P., Chen, B., and Staebler, R. M.: Leaf chlorophyll content as a proxy for leaf photosynthetic capacity, Glob. Change Biol., 23, 3513–3524, https://doi.org/10.1111/gcb.13599, 2017.
- Croft, H., Chen, J., Wang, R., Mo, G., Luo, S., Luo, X., He, L., Gonsamo, A., Arabian, J., Zhang, Y., Simic-Milas, A., Noland, T., He, Y., Homolová, L., Malenovský, Z., Yi, Q., Beringer, J., Amiri, R., Hutley, L., Arellano, P., Stahl, C., and Bonal, D.: The global distribution of leaf chlorophyll content, Remote Sens. Environ., 236, 111479, https://doi.org/10.1016/j.rse.2019.111479, 2020.
- Davies-Barnard, T. and Friedlingstein, P.: The global distribution of biological nitrogen fixation in terrestrial natural ecosystems, Global Biogeochem. Cy., 34, e2019GB006387, https://doi.org/10.1029/2019GB006387, 2020.
- Davies-Barnard, T., Meyerholt, J., Zaehle, S., Friedlingstein, P.,
 Brovkin, V., Fan, Y., Fisher, R. A., Jones, C. D., Lee, H., Peano,
 D., Smith, B., Wårlind, D., and Wiltshire, A. J.: Nitrogen cycling in CMIP6 land surface models: progress and limitations,
 Biogeosciences, 17, 5129–5148, https://doi.org/10.5194/bg-17-5129-2020, 2020.
- Dechant, B., Kattge, J., Pavlick, R., Schneider, F. D., Sabatini, F. M., Moreno-Martínez, Á., Butler, E. E., van Bodegom, P. M., Vallicrosa, H., Kattenborn, T., Boonman, C. C., Madani, N., Wright, I. J., Dong, N., Feilhauer, H., Peñuelas, J., Sardans, J., Aguirre-Gutiérrez, J., Reich, P. B., Leitão, P. J., Cavender-Bares, J., Myers-Smith, I. H., Durán, S. M., Croft, H., Prentice, I. C., Huth, A., Rebel, K., Zaehle, S., Šímová, I., Díaz, S., Reichstein, M., Schiller, C., Bruelheide, H., Mahecha, M., Wirth, C., Malhi, Y., and Townsend, P. A.: Intercomparison of global foliar trait maps reveals fundamental differences and limitations of upscaling approaches, Remote Sens. Environ., 311, 114276, https://doi.org/10.1016/j.rse.2024.114276, 2024.

- ESA: Land Cover CCI Product User Guide Version 2. Tech. Rep., http://maps.elie.ucl.ac.be/CCI/viewer/download/ ESACCI-LC-Ph2-PUGv2_2.0.pdf (last access: 12 February 2025), 2017.
- Evans, J. R.: Photosynthesis and nitrogen relationships in leaves of C3 plants, Oecologia, 78, 9–19, https://doi.org/10.1007/BF00377192, 1989.
- Evans, J. R. and Clarke, V. C.: The nitrogen cost of photosynthesis, J. Exp. Bot., 70, 7–15, https://doi.org/10.1093/jxb/ery366, 2019.
- Famiglietti, C. A., Smallman, T. L., Levine, P. A., Flack-Prain, S., Quetin, G. R., Meyer, V., Parazoo, N. C., Stettz, S. G., Yang, Y., Bonal, D., Bloom, A. A., Williams, M., and Konings, A. G.: Optimal model complexity for terrestrial carbon cycle prediction, Biogeosciences, 18, 2727–2754, https://doi.org/10.5194/bg-18-2727-2021, 2021.
- Fang, H., Jiang, C., Li, W., Wei, S., Baret, F., Chen, J. M., Garcia-Haro, J., Liang, S., Liu, R., Myneni, R. B., Pinty, B., Xiao, Z., and Zhu, Z.: Characterization and intercomparison of global moderate resolution leaf area index (LAI) products: analysis of climatologies and theoretical uncertainties, J. Geophys. Res.-Biogeo., 118, 529–548, https://doi.org/10.1002/jgrg.20051, 2013.
- Farella, M. M., Barnes, M. L., Breshears, D. D., Mitchell, J., van Leeuwen, W. J. D., and Gallery, R. E.: Evaluation of vegetation indices and imaging spectroscopy to estimate foliar nitrogen across disparate biomes, Ecosphere, 13, e3992, https://doi.org/10.1002/ecs2.3992, 2022.
- Farquhar, G. D., von Caemmerer, S., and Berry, J. A.: A biochemical model of photosynthetic CO₂ assimilation in leaves of C3 species, Planta, 149, 78–90, https://doi.org/10.1007/BF00386231, 1980.
- Fisher, J. B., Badgley, G., and Blyth, E.: Global nutrient limitation in terrestrial vegetation, Global Biogeochem. Cy., 26, https://doi.org/10.1029/2011GB004252, 2012.
- Fisher, R. A. and Koven, C. D.: Perspectives on the future of land surface models and the challenges of representing complex terrestrial systems, J. Adv. Model. Earth Sy., 12, e2018MS001453, https://doi.org/10.1029/2018MS001453, 2020.
- FLUXNET: La Thuile Synthesis Dataset, FLUXNET [data set], https://fluxnet.org/data/la-thuile-dataset/ (last access: 12 February 2025), 2024.
- Friedlingstein, P., Jones, M. W., O'Sullivan, M., Andrew, R. M., Hauck, J., Peters, G. P., Peters, W., Pongratz, J., Sitch, S., Le Quéré, C., Bakker, D. C. E., Canadell, J. G., Ciais, P., Jackson, R. B., Anthoni, P., Barbero, L., Bastos, A., Bastrikov, V., Becker, M., Bopp, L., Buitenhuis, E., Chandra, N., Chevallier, F., Chini, L. P., Currie, K. I., Feely, R. A., Gehlen, M., Gilfillan, D., Gkritzalis, T., Goll, D. S., Gruber, N., Gutekunst, S., Harris, I., Haverd, V., Houghton, R. A., Hurtt, G., Ilyina, T., Jain, A. K., Joetzjer, E., Kaplan, J. O., Kato, E., Klein Goldewijk, K., Korsbakken, J. I., Landschützer, P., Lauvset, S. K., Lefèvre, N., Lenton, A., Lienert, S., Lombardozzi, D., Marland, G., McGuire, P. C., Melton, J. R., Metzl, N., Munro, D. R., Nabel, J. E. M. S., Nakaoka, S.-I., Neill, C., Omar, A. M., Ono, T., Peregon, A., Pierrot, D., Poulter, B., Rehder, G., Resplandy, L., Robertson, E., Rödenbeck, C., Séférian, R., Schwinger, J., Smith, N., Tans, P. P., Tian, H., Tilbrook, B., Tubiello, F. N., van der Werf, G. R., Wiltshire, A. J., and Zaehle, S.: Global Carbon Budget 2019, Earth Syst. Sci. Data, 11, 1783-1838, https://doi.org/10.5194/essd-11-1783-2019, 2019.

- Friedlingstein, P., O'Sullivan, M., Jones, M. W., Andrew, R. M., Bakker, D. C. E., Hauck, J., Landschützer, P., Le Quéré, C., Luijkx, I. T., Peters, G. P., Peters, W., Pongratz, J., Schwingshackl, C., Sitch, S., Canadell, J. G., Ciais, P., Jackson, R. B., Alin, S. R., Anthoni, P., Barbero, L., Bates, N. R., Becker, M., Bellouin, N., Decharme, B., Bopp, L., Brasika, I. B. M., Cadule, P., Chamberlain, M. A., Chandra, N., Chau, T.-T.-T., Chevallier, F., Chini, L. P., Cronin, M., Dou, X., Enyo, K., Evans, W., Falk, S., Feely, R. A., Feng, L., Ford, D. J., Gasser, T., Ghattas, J., Gkritzalis, T., Grassi, G., Gregor, L., Gruber, N., Gürses, Ö., Harris, I., Hefner, M., Heinke, J., Houghton, R. A., Hurtt, G. C., Iida, Y., Ilyina, T., Jacobson, A. R., Jain, A., Jarníková, T., Jersild, A., Jiang, F., Jin, Z., Joos, F., Kato, E., Keeling, R. F., Kennedy, D., Klein Goldewijk, K., Knauer, J., Korsbakken, J. I., Körtzinger, A., Lan, X., Lefèvre, N., Li, H., Liu, J., Liu, Z., Ma, L., Marland, G., Mayot, N., McGuire, P. C., McKinley, G. A., Meyer, G., Morgan, E. J., Munro, D. R., Nakaoka, S.-I., Niwa, Y., O'Brien, K. M., Olsen, A., Omar, A. M., Ono, T., Paulsen, M., Pierrot, D., Pocock, K., Poulter, B., Powis, C. M., Rehder, G., Resplandy, L., Robertson, E., Rödenbeck, C., Rosan, T. M., Schwinger, J., Séférian, R., Smallman, T. L., Smith, S. M., Sospedra-Alfonso, R., Sun, Q., Sutton, A. J., Sweeney, C., Takao, S., Tans, P. P., Tian, H., Tilbrook, B., Tsujino, H., Tubiello, F., van der Werf, G. R., van Ooijen, E., Wanninkhof, R., Watanabe, M., Wimart-Rousseau, C., Yang, D., Yang, X., Yuan, W., Yue, X., Zaehle, S., Zeng, J., and Zheng, B.: Global Carbon Budget 2023, Earth Syst. Sci. Data, 15, 5301-5369, https://doi.org/10.5194/essd-15-5301-2023, 2023.
- Friend, A., Stevens, A., Knox, R., and Cannell, M.: A process-based, terrestrial biosphere model of ecosystem dynamics (Hybrid v3.0), Ecol. Model., 95, 249–287, https://doi.org/10.1016/S0304-3800(96)00034-8, 1997.
- Friend, A. D., Geider, R. J., Behrenfeld, M. J., and Still, C. J.: Photosynthesis in global-scale models, in: Photosynthesis in Silico: Understanding Complexity from Molecules to Ecosystems, edited by: Laisk, A., Nedbal, L., and Govindjee, Springer Netherlands, Dordrecht, https://doi.org/10.1007/978-1-4020-9237-4_20, 465-497, 2009.
- Georgievski, G. and Hagemann, S.: Characterizing uncertainties in the ESA-CCI land cover map of the epoch 2010 and their impacts on MPI-ESM climate simulations, Theor. Appl. Climatol., 137, 1587–1603, https://doi.org/10.1007/s00704-018-2675-2, 2019.
- Giannico, V., Chen, J., Shao, C., Ouyang, Z., John, R., and Lafortezza, R.: Contributions of landscape heterogeneity within the footprint of eddy-covariance towers to flux measurements, Agr. Forest Meteorol., 260–261, 144–153, https://doi.org/10.1016/j.agrformet.2018.06.004, 2018.
- Griebel, A., Bennett, L. T., Metzen, D., Cleverly, J., Burba, G., and Arndt, S. K.: Effects of inhomogeneities within the flux footprint on the interpretation of seasonal, annual, and interannual ecosystem carbon exchange, Agr. Forest Meteorol., 221, 50–60, https://doi.org/10.1016/j.agrformet.2016.02.002, 2016.
- Harris, C.: CRU JRA v2.1: A forcings dataset of gridded land surfaceblend of Climatic Research Unit (CRU) and Japanese reanalysis (JRA) data, Centre for Environmental Data Analysis [data set], https://catalogue.ceda.ac.uk/uuid/10d2c73e5a7d46f4ada08b0a26302ef7 (last access: 6 October 2025), 2020.

- Hastie, T., Tibshirani, R., and Friedman, J.: The Elements of Statistical Learning: Data Mining, Inference, and Prediction, 2nd edn., Springer, (corrected 7th printing of Springer Series in Statistics), https://doi.org/10.1007/978-0-387-84858-7, 2009.
- Heiskanen, J., Rautiainen, M., Stenberg, P., Mõttus, M., Vesanto, V.-H., Korhonen, L., and Majasalmi, T.: Seasonal variation in MODIS LAI for a boreal forest area in Finland, Remote Sens. Environ., 126, 104–115, https://doi.org/10.1016/j.rse.2012.08.001, 2012.
- Hengl, T., Mendes de Jesus, J., Heuvelink, G. B. M., Ruiperez Gonzalez, M., Kilibarda, M., Blagotić, A., Shangguan, W., Wright, M. N., Geng, X., Bauer-Marschallinger, B., Guevara, M. A., Vargas, R., MacMillan, R. A., Batjes, N. H., Leenaars, J. G. B., Ribeiro, E., Wheeler, I., Mantel, S., and Kempen, B.: SoilGrids250m: global gridded soil information based on machine learning, PLoS One, 12, 1–40, https://doi.org/10.1371/journal.pone.0169748, 2017.
- Houborg, R., Cescatti, A., Migliavacca, M., and Kustas, W.: Satellite retrievals of leaf chlorophyll and photosynthetic capacity for improved modeling of GPP, Agr. Forest Meteorol., 177, 10–23, https://doi.org/10.1016/j.agrformet.2013.04.006, 2013.
- Howell, T., Meek, D., and Hatfield, J.: Relationship of photosynthetically active radiation to shortwave radiation in the San Joaquin Valley, Agricultural Meteorology, 28, 157–175, https://doi.org/10.1016/0002-1571(83)90005-5, 1983.
- Isaac, P., Cleverly, J., McHugh, I., van Gorsel, E., Ewenz, C., and Beringer, J.: OzFlux data: network integration from collection to curation, Biogeosciences, 14, 2903–2928, https://doi.org/10.5194/bg-14-2903-2017, 2017.
- Jacquemoud, S. and Baret, F.: PROSPECT: a model of leaf optical properties spectra, Remote Sens. Environ., 34, 75–91, https://doi.org/10.1016/0034-4257(90)90100-Z, 1990.
- Joshi, R. K., Gupta, R., Mishra, A., and Garkoti, S. C.: Seasonal variations of leaf ecophysiological traits and strategies of co-occurring evergreen and deciduous trees in white oak forest in the central Himalaya, Environ. Monit. Assess., 196, 634, https://doi.org/10.1007/s10661-024-12771-3, 2024.
- Katahata, S.-I., Naramoto, M., Kakubari, Y., and Mukai, Y.: Seasonal changes in photosynthesis and nitrogen allocation in leaves of different ages in evergreen understory shrub Daphniphyllum humile, Trees, 21, 619–629, https://doi.org/10.1007/s00468-007-0155-x, 2007.
- Kattge, J., Díaz, S., Lavorel, S., Prentice, I. C., Leadley, P., Bönisch, G., Garnier, E., Westoby, M., Reich, P. B., Wright, I. J., Cornelissen, J. H. C., Violle, C., Harrison, S. P., Van Bodegom, P. M., Reichstein, M., Enquist, B. J., Soudzilovskaia, N. A., Ackerly, D. D., Anand, M., Atkin, O., Bahn, M., Baker, T. R., Baldocchi, D., Bekker, R., Blanco, C. C., Blonder, B., Bond, W. J., Bradstock, R., Bunker, D. E., Casanoves, F., Cavender-bares, J., Chambers, J. Q., Chapin Iii, F. S., Chave, J., Coomes, D., Cornwell, W. K., Craine, J. M., Dobrin, B. H., Duarte, L., Durka, W., Elser, J., Esser, G., Estiarte, M., Fagan, W. F., Fang, J., Fernández-méndez, F., Fidelis, A., Finegan, B., Flores, O., Ford, H., Frank, D., Freschet, G. T., Fyllas, N. M., Gallagher, R. V., Green, W. A., Gutierrez, A. G., Hickler, T., Higgins, S. I., Hodgson, J. G., Jalili, A., Jansen, S., Joly, C. A., Kerkhoff, A. J., Kirkup, D., Kitajima, K., Kleyer, M., Klotz, S., Knops, J. M. H., Kramer, K., Kühn, I., Kurokawa, H., Laughlin, D., Lee, T. D., Leishman, M., Lens, F., Lenz, T.,

- Lewis, S. L., Lloyd, J., Llusiá, J., Louault, F., Ma, S., Mahecha, M. D., Manning, P., Massad, T., Medlyn, B. E., Messier, J., Moles, A. T., Müller, S. C., Nadrowski, K., Naeem, S., Niinemets, Ü., Nöllert, S., Nüske, A., Ogaya, R., Oleksyn, J., Onipchenko, V. G., Onoda, Y., Ordoñez, J., Overbeck, G., Ozinga, W. A., Patiño, S., Paula, S., Pausas, J. G., Peñuelas, J., Phillips, O. L., Pillar, V., Poorter, H., Poorter, L., Poschlod, P., Prinzing, A., Proulx, R., Rammig, A., Reinsch, S., Reu, B., Sack, L., Salgado-negret, B., Sardans, J., Shiodera, S., Shipley, B., Siefert, A., Sosinski, E., Soussana, J.-f., Swaine, E., Swenson, N., Thompson, K., Thornton, P., Waldram, M., Weiher, E., White, M., White, S., Wright, S. J., Yguel, B., Zaehle, S., Zanne, A. E., and Wirth, C.: TRY a global database of plant traits, Glob. Change Biol., 17, 2905–2935, https://doi.org/10.1111/j.1365-2486.2011.02451.x, 2011.
- Kooistra, L., Berger, K., Brede, B., Graf, L. V., Aasen, H., Roujean, J.-L., Machwitz, M., Schlerf, M., Atzberger, C., Prikaziuk, E., Ganeva, D., Tomelleri, E., Croft, H., Reyes Muñoz, P., Garcia Millan, V., Darvishzadeh, R., Koren, G., Herrmann, I., Rozenstein, O., Belda, S., Rautiainen, M., Rune Karlsen, S., Figueira Silva, C., Cerasoli, S., Pierre, J., Tanır Kayıkçı, E., Halabuk, A., Tunc Gormus, E., Fluit, F., Cai, Z., Kycko, M., Udelhoven, T., and Verrelst, J.: Reviews and syntheses: Remotely sensed optical time series for monitoring vegetation productivity, Biogeosciences, 21, 473–511, https://doi.org/10.5194/bg-21-473-2024, 2024.
- Kou-Giesbrecht, S., Arora, V. K., Seiler, C., Arneth, A., Falk, S., Jain, A. K., Joos, F., Kennedy, D., Knauer, J., Sitch, S., O'Sullivan, M., Pan, N., Sun, Q., Tian, H., Vuichard, N., and Zaehle, S.: Evaluating nitrogen cycling in terrestrial biosphere models: a disconnect between the carbon and nitrogen cycles, Earth Syst. Dynam., 14, 767–795, https://doi.org/10.5194/esd-14-767-2023, 2023.
- Kull, O. and Kruijt, B.: Leaf photosynthetic light response: a mechanistic model for scaling photosynthesis to leaves and canopies, Funct. Ecol., 12, 767–777, 1998.
- Laitinen, K., Luomala, E.-M., Kellomäki, S., and Vapaavuori, E.: Carbon assimilation and nitrogen in needles of fertilized and unfertilized field-grown Scots pine at natural and elevated concentrations of CO₂, Tree Physiology, 20, 881–892, https://doi.org/10.1093/treephys/20.13.881, 2000.
- Lamarque, J.-F., Bond, T. C., Eyring, V., Granier, C., Heil, A., Klimont, Z., Lee, D., Liousse, C., Mieville, A., Owen, B., Schultz, M. G., Shindell, D., Smith, S. J., Stehfest, E., Van Aardenne, J., Cooper, O. R., Kainuma, M., Mahowald, N., McConnell, J. R., Naik, V., Riahi, K., and van Vuuren, D. P.: Historical (1850–2000) gridded anthropogenic and biomass burning emissions of reactive gases and aerosols: methodology and application, Atmos. Chem. Phys., 10, 7017–7039, https://doi.org/10.5194/acp-10-7017-2010, 2010.
- Lamarque, J.-F., Kyle, G. P., Meinshausen, M., Riahi, K., Smith, S. J., van Vuuren, D. P., Conley, A. J., and Vitt, F.: Global and regional evolution of short-lived radiatively-active gases and aerosols in the Representative Concentration Pathways, Climatic Change, 109, 191, https://doi.org/10.1007/s10584-011-0155-0, 2011.
- LeBauer, D. S. and Treseder, K. K.: Nitrogen limitation of net primary productivity in terrestrial ecosystems is globally distributed, Ecology, 89, 371–379, 2008.

- Linkosalmi, M., Aurela, M., Tuovinen, J.-P., Peltoniemi, M., Tanis, C. M., Arslan, A. N., Kolari, P., Böttcher, K., Aalto, T., Rainne, J., Hatakka, J., and Laurila, T.: Digital photography for assessing the link between vegetation phenology and CO₂ exchange in two contrasting northern ecosystems, Geosci. Instrum. Method. Data Syst., 5, 417–426, https://doi.org/10.5194/gi-5-417-2016, 2016.
- Liu, Y., Chen, J. M., He, L., Wang, R., Smith, N. G., Keenan, T. F., Rogers, C., Li, W., and Leng, J.: Global photosynthetic capacity of C3 biomes retrieved from solar-induced chlorophyll fluorescence and leaf chlorophyll content, Remote Sens. Environ., 287, 113457, https://doi.org/10.1016/j.rse.2023.113457, 2023.
- Lu, X., Ju, W., Li, J., Croft, H., Chen, J. M., Luo, Y., Yu, H., and Hu, H.: Maximum carboxylation rate estimation with chlorophyll content as a proxy of Rubisco content, J. Geophys. Res.-Biogeo., 125, e2020JG005748, https://doi.org/10.1029/2020JG005748, 2020.
- Lu, X., Croft, H., Chen, J. M., Luo, Y., and Ju, W.: Estimating photosynthetic capacity from optimized Rubisco-chlorophyll relationships among vegetation types and under global change, Environ. Res. Lett., 17, 014028, https://doi.org/10.1088/1748-9326/ac444d, 2022.
- Lundberg, S. M. and Lee, S.-I.: A unified approach to interpreting model predictions, in: Advances in Neural Information Processing Systems 30, edited by: Guyon, I., Luxburg, U. V., Bengio, S., Wallach, H., Fergus, R., Vishwanathan, S., and Garnett, R., Curran Associates, Inc., http://papers.nips.cc/paper/7062-a-unified-approach-to-interpreting-model-predictions.pdf (last access: 6 October 2025), 4765–4774, 2017.
- Luo, X., Croft, H., Chen, J. M., Bartlett, P., Staebler, R., and Froelich, N.: Incorporating leaf chlorophyll content into a twoleaf terrestrial biosphere model for estimating carbon and water fluxes at a forest site, Agr. Forest Meteorol., 248, 156–168, https://doi.org/10.1016/j.agrformet.2017.09.012, 2018.
- Luo, X., Croft, H., Chen, J. M., He, L., and Keenan, T. F.: Improved estimates of global terrestrial photosynthesis using information on leaf chlorophyll content, Glob. Change Biol., 25, 2499–2514, https://doi.org/10.1111/gcb.14624, 2019.
- Luo, X., Keenan, T. F., Chen, J. M., Croft, H., Colin Prentice, I., Smith, N. G., Walker, A. P., Wang, H., Wang, R., Xu, C., and Zhang, Y.: Global variation in the fraction of leaf nitrogen allocated to photosynthesis, Nat. Commun., 12, 4866, https://doi.org/10.1038/s41467-021-25163-9, 2021.
- Medlyn, B. E., Zaehle, S., De Kauwe, M. G., Walker, A. P., Dietze, M. C., Hanson, P. J., Hickler, T., Jain, A. K., Luo, Y., Parton, W., Prentice, I. C., Thornton, P. E., Wang, S., Wang, Y.-P., Weng, E., Iversen, C. M., McCarthy, H. R., Warren, J. M., Oren, R., and Norby, R. J.: Using ecosystem experiments to improve vegetation models, Nat. Clim. Change, 5, 528–534, https://doi.org/10.1038/nclimate2621, 2015.
- Meyerholt, J., Sickel, K., and Zaehle, S.: Ensemble projections elucidate effects of uncertainty in terrestrial nitrogen limitation on future carbon uptake, Glob. Change Biol., 26, 3978–3996, https://doi.org/10.1111/gcb.15114, 2020.
- Miinalainen, T.: Data for the manuscript 'Evaluating the carbon and nitrogen cycles of the QUINCY terrestrial biosphere model using space-born optical remotely-sensed data', Finnish Meteorological Institute [data set], https://doi.org/10.57707/FMI-B2SHARE.F8AB5F4ED6534B1597A2DB73CC5175FF, 2025.

- Nabuurs, G.-J., Mrabet, R., Hatab, A. A., Bustamante, M., Clark, H., Havlík, P., House, J., Mbow, C., Ninan, K., Popp, A., Roe, S., Sohngen, B., and Towprayoo, S.: Agriculture, Forestry and Other Land Uses (AFOLU), in: Climate Change 2022: Mitigation of Climate Change. Contribution of Working Group III to the Sixth Assessment Report of the Intergovernmental Panel on Climate Change, edited by: Shukla, P., Skea, J., Slade, R., Khourdajie, A. A., van Diemen, R., McCollum, D., Pathak, M., Some, S., Vyas, P., Fradera, R., Belkacemi, M., Hasija, A., Lisboa, G., Luz, S., and Malley, J., Cambridge University Press, Cambridge, UK and New York, NY, USA, https://doi.org/10.1017/9781009157926.009, 2022.
- Niinemets, Ü., Kull, O., and Tenhunen, J. D.: An analysis of light effects on foliar morphology, physiology, and light interception in temperate deciduous woody species of contrasting shade tolerance, Tree Physiology, 18, 681–696, https://doi.org/10.1093/treephys/18.10.681, 1998.
- Onoda, Y., Wright, I. J., Evans, J. R., Hikosaka, K., Kitajima, K., Niinemets, Ü., Poorter, H., Tosens, T., and Westoby, M.: Physiological and structural tradeoffs underlying the leaf economics spectrum, New Phytol., 214, 1447–1463, https://doi.org/10.1111/nph.14496, 2017.
- Parton, W. J., Scurlock, J. M. O., Ojima, D. S., Gilmanov, T. G., Scholes, R. J., Schimel, D. S., Kirchner, T., Menaut, J.-C., Seastedt, T., Garcia Moya, E., Kamnalrut, A., and Kinyamario, J. I.: Observations and modeling of biomass and soil organic matter dynamics for the grassland biome worldwide, Global Biogeochem. Cy., 7, 785–809, https://doi.org/10.1029/93GB02042, 1993.
- Pastorello, G., Trotta, C., Canfora, E., Chu, H., Christianson, D., Cheah, Y.-W., Poindexter, C., Chen, J., Elbashandy, A., Humphrey, M., Isaac, P., Polidori, D., Reichstein, M., Ribeca, A., van Ingen, C., Vuichard, N., Zhang, L., Amiro, B., Ammann, C., Arain, M. A., Ardö, J., Arkebauer, T., Arndt, S. K., Arriga, N., Aubinet, M., Aurela, M., Baldocchi, D., Barr, A., Beamesderfer, E., Marchesini, L. B., Bergeron, O., Beringer, J., Bernhofer, C., Berveiller, D., Billesbach, D., Black, T. A., Blanken, P. D., Bohrer, G., Boike, J., Bolstad, P. V., Bonal, D., Bonnefond, J.-M., Bowling, D. R., Bracho, R., Brodeur, J., Brümmer, C., Buchmann, N., Burban, B., Burns, S. P., Buysse, P., Cale, P., Cavagna, M., Cellier, P., Chen, S., Chini, I., Christensen, T. R., Cleverly, J., Collalti, A., Consalvo, C., Cook, B. D., Cook, D., Coursolle, C., Cremonese, E., Curtis, P. S., D'Andrea, E., da Rocha, H., Dai, X., Davis, K. J., Cinti, B. D., Grandcourt, A. d., Ligne, A. D., De Oliveira, R. C., Delpierre, N., Desai, A. R., Di Bella, C. M., Di Tommasi, P., Dolman, H., Domingo, F., Dong, G., Dore, S., Duce, P., Dufrêne, E., Dunn, A., Dušek, J., Eamus, D., Eichelmann, U., ElKhidir, H. A. M., Eugster, W., Ewenz, C. M., Ewers, B., Famulari, D., Fares, S., Feigenwinter, I., Feitz, A., Fensholt, R., Filippa, G., Fischer, M., Frank, J., Galvagno, M., Gharun, M., Gianelle, D., Gielen, B., Gioli, B., Gitelson, A., Goded, I., Goeckede, M., Goldstein, A. H., Gough, C. M., Goulden, M. L., Graf, A., Griebel, A., Gruening, C., Grünwald, T., Hammerle, A., Han, S., Han, X., Hansen, B. U., Hanson, C., Hatakka, J., He, Y., Hehn, M., Heinesch, B., Hinko-Najera, N., Hörtnagl, L., Hutley, L., Ibrom, A., Ikawa, H., Jackowicz-Korczynski, M., Janouš, D., Jans, W., Jassal, R., Jiang, S., Kato, T., Khomik, M., Klatt, J., Knohl, A., Knox, S., Kobayashi, H., Koerber, G.,

- Kolle, O., Kosugi, Y., Kotani, A., Kowalski, A., Kruijt, B., Kurbatova, J., Kutsch, W. L., Kwon, H., Launiainen, S., Laurila, T., Law, B., Leuning, R., Li, Y., Liddell, M., Limousin, J.-M., Lion, M., Liska, A. J., Lohila, A., López-Ballesteros, A., López-Blanco, E., Loubet, B., Loustau, D., Lucas-Moffat, A., Lüers, J., Ma, S., Macfarlane, C., Magliulo, V., Maier, R., Mammarella, I., Manca, G., Marcolla, B., Margolis, H. A., Marras, S., Massman, W., Mastepanov, M., Matamala, R., Matthes, J. H., Mazzenga, F., McCaughey, H., McHugh, I., McMillan, A. M. S., Merbold, L., Meyer, W., Meyers, T., Miller, S. D., Minerbi, S., Moderow, U., Monson, R. K., Montagnani, L., Moore, C. E., Moors, E., Moreaux, V., Moureaux, C., Munger, J. W., Nakai, T., Neirynck, J., Nesic, Z., Nicolini, G., Noormets, A., Northwood, M., Nosetto, M., Nouvellon, Y., Novick, K., Oechel, W., Olesen, J. E., Ourcival, J.-M., Papuga, S. A., Parmentier, F.-J., Paul-Limoges, E., Pavelka, M., Peichl, M., Pendall, E., Phillips, R. P., Pilegaard, K., Pirk, N., Posse, G., Powell, T., Prasse, H., Prober, S. M., Rambal, S., Rannik, Ü., Raz-Yaseef, N., Rebmann, C., Reed, D., Dios, V. R. d., Restrepo-Coupe, N., Reverter, B. R., Roland, M., Sabbatini, S., Sachs, T., Saleska, S. R., Sánchez-Cañete, E. P., Sanchez-Mejia, Z. M., Schmid, H. P., Schmidt, M., Schneider, K., Schrader, F., Schroder, I., Scott, R. L., Sedlák, P., Serrano-Ortíz, P., Shao, C., Shi, P., Shironya, I., Siebicke, L., Šigut, L., Silberstein, R., Sirca, C., Spano, D., Steinbrecher, R., Stevens, R. M., Sturtevant, C., Suyker, A., Tagesson, T., Takanashi, S., Tang, Y., Tapper, N., Thom, J., Tomassucci, M., Tuovinen, J.-P., Urbanski, S., Valentini, R., van der Molen, M., van Gorsel, E., van Huissteden, K., Varlagin, A., Verfaillie, J., Vesala, T., Vincke, C., Vitale, D., Vygodskaya, N., Walker, J. P., Walter-Shea, E., Wang, H., Weber, R., Westermann, S., Wille, C., Wofsy, S., Wohlfahrt, G., Wolf, S., Woodgate, W., Li, Y., Zampedri, R., Zhang, J., Zhou, G., Zona, D., Agarwal, D., Biraud, S., Torn, M., and Papale, D.: The FLUXNET2015 dataset and the ONEFlux processing pipeline for eddy covariance data, Scientific Data, 7, 225, https://doi.org/10.1038/s41597-020-0534-3, 2020.
- Pedregosa, F., Varoquaux, G., Gramfort, A., Michel, V., Thirion, B., Grisel, O., Blondel, M., Prettenhofer, P., Weiss, R., Dubourg, V., Vanderplas, J., Passos, A., Cournapeau, D., Brucher, M., Perrot, M., and Duchesnay, E.: Scikit-learn: Machine Learning in Python, J. Mach. Learn. Res., 12, 2825–2830, 2011.
- Peltoniemi, M., Ruhanen, H., Linkosalmi, M., and Aurela, M.: Shoot pigment measurements from Scots pine trees at the Sodankylä eddy-covariance site in 2015, Zenodo [data set], https://doi.org/10.5281/zenodo.17192030, 2025.
- Reyes-Muñoz, P., Pipia, L., Salinero-Delgado, M., Belda, S., Berger, K., Estévez, J., Morata, M., Rivera-Caicedo, J. P., and Verrelst, J.: Quantifying fundamental vegetation traits over Europe using the Sentinel-3 OLCI Catalogue in Google Earth Engine, Remote Sens.-Basel, 14, https://doi.org/10.3390/rs14061347, 2022.
- Reyes-Muñoz, P. and Salinero-Delgado, M.: S3-TOA-GPR-1 vegetation products, GitHub [code], https://github.com/psreyes/S3_TOA_GPR_1 (last access: 6 October 2025), 2022.
- Rogers, A., Medlyn, B. E., Dukes, J. S., Bonan, G., von Caemmerer, S., Dietze, M. C., Kattge, J., Leakey, A. D. B., Mercado, L. M., Niinemets, Ü., Prentice, I. C., Serbin, S. P., Sitch, S., Way, D. A., and Zaehle, S.: A roadmap for improving the repre-

- sentation of photosynthesis in Earth system models, New Phytol., 213, 22–42, https://doi.org/10.1111/nph.14283, 2017.
- Sage, R. F., Pearcy, R. W., and Seemann, J. R.: The nitrogen use efficiency of C3 and C4 plants: III. Leaf nitrogen effects on the activity of carboxylating enzymes in Chenopodium album (L.) and Amaranthus retroflexus (L.), Plant Physiology, 85, 355–359, https://doi.org/10.1104/pp.85.2.355, 1987.
- Sallas, L., Luomala, E.-M., Utriainen, J., Kainulainen, P., and Holopainen, J. K.: Contrasting effects of elevated carbon dioxide concentration and temperature on Rubisco activity, chlorophyll fluorescence, needle ultrastructure and secondary metabolites in conifer seedlings, Tree Physiology, 23, 97–108, https://doi.org/10.1093/treephys/23.2.97, 2003.
- Seiler, C., Kou-Giesbrecht, S., Arora, V. K., and Melton, J. R.: The impact of climate forcing biases and the nitrogen cycle on land carbon balance projections, J. Adv. Model. Earth Sy., 16, e2023MS003749, https://doi.org/10.1029/2023MS003749, 2024.
- Stenberg, P., DeLucia, E. H., Schoettle, A. W., and Smolander, H.: Photosynthetic light capture and processing from cell to canopy, in: Resource Physiology of Conifers, Acquition, Allocation, and Utilization, edited by: Smith, W. K. and Hinckley, T. M., Academic Press, 3rd edn., 3–38, https://doi.org/10.1016/C2009-0-02454-4, 1995.
- Tamm, C. O.: Nitrogen-limited and nitrogen-depleted terrestrial ecosystems: ecological characteristics, in: Nitrogen in Terrestrial Ecosystems: Questions of Productivity, Vegetational Changes, and Ecosystem Stability, Springer Berlin Heidelberg, Berlin, Heidelberg, https://doi.org/10.1007/978-3-642-75168-4_3, 34– 49, 1991.
- Thomas, R. Q., Brookshire, E. N. J., and Gerber, S.: Nitrogen limitation on land: how can it occur in Earth system models?, Glob. Change Biol., 21, 1777–1793, https://doi.org/10.1111/gcb.12813, 2015.
- Thum, T., Aalto, T., Laurila, T., Aurela, M., Kolari, P., and Hari, P.: Parametrization of two photosynthesis models at the canopy scale in a northern boreal Scots pine forest, Tellus B, https://doi.org/10.1111/j.1600-0889.2007.00305.x, 2007.
- Thum, T., Caldararu, S., Engel, J., Kern, M., Pallandt, M., Schnur, R., Yu, L., and Zaehle, S.: A new model of the coupled carbon, nitrogen, and phosphorus cycles in the terrestrial biosphere (QUINCY v1.0; revision 1996), Geosci. Model Dev., 12, 4781–4802, https://doi.org/10.5194/gmd-12-4781-2019, 2019.
- Thum, T., Miinalainen, T., Seppälä, O., Croft, H., Rogers, C., Staebler, R., Caldararu, S., and Zaehle, S.: Modelling decadal trends and the impact of extreme events on carbon fluxes in a temperate deciduous forest using a terrestrial biosphere model, Biogeosciences, 22, 1781–1807, https://doi.org/10.5194/bg-22-1781-2025, 2025.
- Thurner, M., Yu, K., Manzoni, S., Prokushkin, A., Thurner, M. A., Wang, Z., and Hickler, T.: Nitrogen concentrations in boreal and temperate tree tissues vary with tree age/size, growth rate, and climate, Biogeosciences, 22, 1475–1493, https://doi.org/10.5194/bg-22-1475-2025, 2025.
- Tum, M., Günther, K. P., Böttcher, M., Baret, F., Bittner, M., Brockmann, C., and Weiss, M.: Global gap-free MERIS LAI time series (2002–2012), Remote Sens.-Basel, 8, https://doi.org/10.3390/rs8010069, 2016.

- Ukkola, A. M., Abramowitz, G., and De Kauwe, M. G.: A flux tower dataset tailored for land model evaluation, Earth Syst. Sci. Data, 14, 449–461, https://doi.org/10.5194/essd-14-449-2022, 2022.
- Verhoef, W.: Light scattering by leaf layers with application to canopy reflectance modeling: the SAIL model, Remote Sens. Environ., 16, 125–141, https://doi.org/10.1016/0034-4257(84)90057-9, 1984.
- Vicente-Serrano, S. M., Domínguez-Castro, F., Reig, F., Latorre, B., and Beguería, S.: SPEICropDroughtMonitor, Instituto Pirenaico de Ecología (IPE CSIC) and Estación Experimental de Aula Dei (EEAD CSIC) [data set], https://doi.org/10.20350/digitalCSIC/15469, 2023a.
- Vicente-Serrano, S. M., Domínguez-Castro, F., Reig, F., Tomas-Burguera, M., Peña-Angulo, D., Latorre, B., Beguería, S., Rabanaque, I., Noguera, I., Lorenzo-Lacruz, J., and El Kenawy, A.: A global drought monitoring system and dataset based on ERA5 reanalysis: a focus on crop-growing regions, Geosci. Data J., 10, 505–518, https://doi.org/10.1002/gdj3.178, 2023b.
- Vitousek, P. M. and Howarth, R. W.: Nitrogen limitation on land and in the sea: how can it occur?, Biogeochemistry, 13, 87–115, https://doi.org/10.1007/BF00002772, 1991.
- Vuichard, N., Messina, P., Luyssaert, S., Guenet, B., Zaehle, S., Ghattas, J., Bastrikov, V., and Peylin, P.: Accounting for carbon and nitrogen interactions in the global terrestrial ecosystem model ORCHIDEE (trunk version, rev 4999): multi-scale evaluation of gross primary production, Geosci. Model Dev., 12, 4751– 4779, https://doi.org/10.5194/gmd-12-4751-2019, 2019.
- Wang, C., Yang, Y., Yin, G., Xie, Q., Xu, B., Verger, A., Descals, A., Filella, I., and Peñuelas, J.: Divergence in autumn phenology extracted from different satellite proxies reveals the timetable of leaf senescence over deciduous forests, Geophys. Res. Lett., 51, e2023GL107346, https://doi.org/10.1029/2023GL107346, 2024.
- Wang, R., Chen, J. M., Luo, X., Black, A., and Arain, A.: Seasonality of leaf area index and photosynthetic capacity for better estimation of carbon and water fluxes in evergreen conifer forests, Agr. Forest Meteorol., 279, 107708, https://doi.org/10.1016/j.agrformet.2019.107708, 2019.
- Warren, C. R. and Adams, M. A.: Distribution of N, Rubisco and photosynthesis in Pinus pinaster and acclimation to light, Plant, Cell and Environment, 24, 597–609, https://doi.org/10.1046/j.1365-3040.2001.00711.x, 2001.

- Wullschleger, S. D.: Biochemical limitations to carbon assimilation in C3 plants a retrospective analysis of the A/Ci curves from 109 species, J. Exp. Bot., 44, 907–920, https://doi.org/10.1093/jxb/44.5.907, 1993.
- Yasumura, Y. and Ishida, A.: Temporal variation in leaf nitrogen partitioning of a broad-leaved evergreen tree, Quercus myrsinaefolia, Journal of Plant Research, 124, 115–123, https://doi.org/10.1007/s10265-010-0358-x, 2011.
- Zaehle, S., Caldararu, S., Engel, J., Kern, M., Schnur, R., Thum, T., and Yu, L.: QUINCY model, Max Planck Institute for Biogeochemistry [code], https://doi.org/10.17871/quincy-model-2019, 2019.
- Zaehle, S. and Friend, A. D.: Carbon and nitrogen cycle dynamics in the O-CN land surface model: 1. Model description, site-scale evaluation, and sensitivity to parameter estimates, Global Biogeochem. Cy., 24, https://doi.org/10.1029/2009GB003521, 2010.
- Zaehle, S., Medlyn, B. E., De Kauwe, M. G., Walker, A. P., Dietze, M. C., Hickler, T., Luo, Y., Wang, Y.-P., El-Masri, B., Thornton, P., Jain, A., Wang, S., Warlind, D., Weng, E., Parton, W., Iversen, C. M., Gallet-Budynek, A., McCarthy, H., Finzi, A., Hanson, P. J., Prentice, I. C., Oren, R., and Norby, R. J.: Evaluation of 11 terrestrial carbon–nitrogen cycle models against observations from two temperate Free-Air CO₂ Enrichment studies, New Phytol., 202, 803–822, https://doi.org/10.1111/nph.12697, 2014.
- Zhang, C., Atherton, J., Peñuelas, J., Filella, I., Kolari, P., Aalto, J., Ruhanen, H., Bäck, J., and Porcar-Castell, A.: Do all chlorophyll fluorescence emission wavelengths capture the spring recovery of photosynthesis in boreal evergreen foliage?, Plant, Cell and Environment, 42, 3264–3279, https://doi.org/10.1111/pce.13620, 2019.
- Ziehn, T., Wang, Y.-P., and Huang, Y.: Land carbon-concentration and carbon-climate feedbacks are significantly reduced by nitrogen and phosphorus limitation, Environ. Res. Lett., 16, 074043, https://doi.org/10.1088/1748-9326/ac0e62, 2021.